# Impact of Matrix Diffusion on Heat Transport Through Heterogeneous Fractured Aquifers

Silvia de Simone, Olivier Bour, Philippe Davy

AGU ADVANCING EARTH AND SPACE SCIENCE

Water Resources Research

RESEARCH ARTICLE
10.1029/2022WR033910

# Impact of Matrix Diffusion on Heat Transport Through Heterogeneous Fractured Aquifers

**Silvia De Simone[1], Olivier Bour[1], and Philippe Davy[1]**

[1]University Rennes, CNRS, Géosciences Rennes, UMR 6118, Rennes, France

**Key Points:**

- Heat transport in heterogeneous fractured aquifers exhibits post-peak tails that express the characteristics of the fracture network
- DFN simulations show that heat BTC transition into diffusive regime depends whether the system is dominated by large or small fractures
- The combined observation of solute and heat decay rates allows characterizing connectivity structure and fracture aperture variability

**Supporting Information:**

Supporting Information may be found in the online version of this article.

**Correspondence to:**

S. De Simone,
silviadesi@gmail.com

**Citation:**

De Simone, S., Bour, O., & Davy, P. (2023). Impact of matrix diffusion on heat transport through heterogeneous fractured aquifers. *Water Resources Research*, *59*, e2022WR033910. https://doi.org/10.1029/2022WR033910

Received 2 NOV 2022
Accepted 4 FEB 2023

**Author Contributions:**

**Conceptualization:** Silvia De Simone
**Formal analysis:** Silvia De Simone
**Funding acquisition:** Olivier Bour, Philippe Davy
**Methodology:** Silvia De Simone
**Software:** Silvia De Simone
**Supervision:** Olivier Bour, Philippe Davy
**Validation:** Silvia De Simone, Philippe Davy
**Visualization:** Silvia De Simone
**Writing – original draft:** Silvia De Simone
**Writing – review & editing:** Olivier Bour, Philippe Davy



**Abstract** Heat transport in fractured aquifers is determined by the combined effects of flow velocity heterogeneity in the fracture system, and diffusive exchange between the fluid in the fractures and the rock matrix, which can be assumed as impervious. We analyze the impacts of this diffusive exchange on the response to heat transport, as opposite to the pure advective displacement, which governs solute transport. We focus on the post-peak behavior where we observe pre-asymptotic regimes with slopes that differ from the signature of matrix diffusion, which exhibits a decay rate of −3/2. This deviation is driven by the variability of both velocity field and fracture aperture field. We derive theoretical models that predict these pre-asymptotic tails under three extreme cases that can be related with specific network structures, that is, networks dominated by large or small fractures, networks with highly or poorly channelized flow. These theoretical predictions are compared with results from numerical simulations in different sets of three-dimensional discrete fracture networks. We determine that the combined observation of solute and heat transport responses allows classifying the network in terms of connectivity structure, and partially characterizing the fracture aperture variability in terms of upscaled parameters.

## 1. Introduction

Transport in subsurface fractured rocks is strongly affected by the variability of the velocity field, which in complex fracture networks may vary broadly. Because the rock matrix is almost impervious, the flow occurs in the network of connected fractures, which exhibits multiscale features spanning several orders of magnitude, that is, fracture size ranging from millimeters to hundreds of meters, with a small number of fractures acting as preferential flow paths where most of the fluid flow channelizes (Bonnet et al., 2001; Goc et al., 2010; C. F. Tsang & Neretnieks, 1998). Heterogeneity at different scales in fracture aperture and hydraulic conductivity implies strong heterogeneity in flow rates and diffusive processes, leading to behaviors that cannot be captured by traditional theories, and field-scale observations that are difficult to predict (Becker & Shapiro, 2003). Understanding the impact of multiscale heterogeneity and network connectivity on advective and advective-diffusive transport is critical for many scientific and engineering applications including geothermal energy, nuclear waste disposal, waste-water injection, and water resource protection. It is key to improve our capacity of characterizing the geometry of the fracture network and identifying connected structures by means of field tests, such as conservative solute or heat tracer experiments. They typically comprise the interpretation of breakthrough curves (BTCs) to yield information on the structure of the fractured systems which drive flow and transport processes.

In natural fractured media, transport of both solutes and heat behaves different from traditional Fickian models, where a constant dispersion coefficient can describe the impact of flow fluctuations occurring at the small scales on solute and thermal spreading. Solute transport through fractured media often exhibits anomalous (non-Fickian) behavior, with non-symmetrical BTCs characterized by power-law post-peak tails (Berkowitz & Scher, 1995). This behavior is mostly controlled by the structure of the interconnected network rather than by the variability in fracture aperture, the latter leading to local flow fluctuations within an individual fracture, but not significantly influencing flow, and thus advective transport, at the network scale (Frampton et al., 2019; Makedonska et al., 2016). Yet, linking structural and hydrodynamic properties to large-scale transport behavior is challenging because of the complexity of the fracture network (Hyman, Dentz et al., 2019a, 2019b; Kang et al., 2020).

Besides the heterogeneity of advective displacement, transport is also affected by diffusive exchange between the fluid circulating in the fractures and the rock matrix, which can be assumed as a non-flowing (or immobile) region. While molecular diffusion of solutes has negligible effects on the observed response (Becker & Shapiro, 2000), in the case of heat transport the fluid-rock diffusive exchange strongly modifies the BTC (Carrera et al., 1998),

resulting in delayed peaks and different post-peak tailings, as also highlighted by field tests combining solute and heat tracers (de La Bernardie et al., 2018; Klepikova et al., 2016). In the classical model of flow into a single fracture with diffusion into the adjacent semi-infinite rock matrix, the post-peak tail exhibits a decay exponent equal to −3/2 (Neretnieks, 1980; Tang et al., 1981). However, the interaction between matrix diffusion and in-fracture heterogeneous advection leads to BTCs with late-time exponents different from −3/2, as illustrated by means of different approaches including multi-rate mass transfer (Carrera et al., 1998; Haggerty et al., 2000; Haggerty & Gorelick, 1995), continuous time random walk (CTRW) combined with a stochastic representation of the matrix trapping times (Comolli et al., 2016; Dentz et al., 2012) and discrete fracture network (DFN) modeling (Frampton & Cvetkovic, 2007; Hyman, Rajaram et al., 2019; Painter et al., 2002).

Numerical experiments with DFNs allow deeply analyzing these combined processes under several scenarios. In the DFN approach, the medium is represented by a set of interconnected fractures in which flow and transport are calculated. Given the difficulty of describing intensely fractured aquifers, the DFN method represents a powerful tool as it builds on the stochastic generation of the fractured system according to the statistic distribution of some attributes, such as the fracture size, orientation, transmissivity and density. Hyman, Rajaram et al. (2019) use numerical simulations in three-dimensional DFNs and theoretical considerations to illustrate that the late-time decay rate of BTCs deviates from the classical diffusive behavior if the advective travel time distribution decays relatively slowly. However, they limit the analysis to the case of homogeneous fracture aperture. Hyman and Dentz (2021) extended this work to analyze the impact of fracture aperture variability on BTCs resulting from advective transport within the fractures with transverse diffusion into the adjacent matrix. They make use of DFN simulations to calibrate an upscaled model that combine the CTRW approach, reproducing the advective transport, with a compound Poisson process that quantifies the trapping time in the rock matrix.

Defining a relationship between the characteristics of the fractured medium and the observed BTC remains, however, a critical open challenge. Here we analyze the impact of matrix diffusion with fracture aperture variability on the breakthrough tail, to study how the combined use of solute and heat tracer tests may reveal characteristics of the network. The heterogeneous properties of the fractured system are linked to its upscaled characteristics and consequent BTC observations, which represents the main novelty of this paper.

We first analyze the parameters governing the advective transport with transverse diffusion in heterogeneous fractured rocks, with emphasis on the late time tail. Based on these considerations, we define a theoretical framework describing the response to solute and heat transport under three conditions that represent different network structures. We test this framework against results from numerical simulations on three-dimensional DFNs, where the advective transport is modeled by means of Lagrangian particle tracking, while the diffusive contribution is analytically estimated on each particle trajectory under the assumption of semi-infinite matrix. Results from numerical simulations allow us to analyze the link between the observed BTC, the upscaled parameters and the characteristics of the complex fractured medium. Finally, we propose a novel approach for the characterization of fractured aquifers in terms of upscaled parameters and connectivity level, which is based on the combined observations of BTCs from solute and heat tracer tests.

## 2. Theory

We consider a fractured aquifer with steady state groundwater flow. Both fluid and rock are considered incompressible. A conservative tracer (either a solute mass or heat) is instantaneously released at the inlet boundary $x = 0$, and its arrival is observed at a cross control section placed at the distance $x = X$. A constant hydraulic gradient is assumed between the boundaries $x = 0$ and $x = X$. We assume that the fluid flow occurs exclusively in the fracture network while the matrix is impermeable. Fracture planes are assimilated to parallel plates and lubrication approximation is assumed, thus the cubic law holds locally (Méheust & Schmittbuhl, 2001; Witherspoon et al., 1980; Zimmerman & Bodvarsson, 1996). Because of these assumptions, the derivations in the following are made in terms of hydraulic aperture, which may be smaller than the true (mechanical) aperture (Renshaw, 1995). For the sake of completeness, we start by assuming that both solute and heat tracers are displaced downstream by fluid advection within the fracture system with a diffusive exchange taking place between the fluid in the fractures and the rock matrix. Diffusive transport in the rock mostly occurs in the direction orthogonal to the fracture. Lateral and longitudinal diffusions are disregarded both in the fracture and in the matrix. Since fracture thickness is small, complete mixing occurs, which means flat solute and temperature profiles along the fracture thickness. The matrix is assumed as semi-infinite in the direction normal to the fracture, which is mostly

valid for short times. A consequence of this assumption is that the tracer cannot displace from one fracture to another throughout the matrix. Solutions that overcome the above-mentioned limitations are provided in Sudicky and Frind (1982); Roubinet et al. (2012); and Dejam et al. (2014), where the effects of parallel neighboring fractures, two-dimensional diffusive transport in the fracture and in the matrix, and incomplete mixing in the fracture width are analyzed.

The conceptualization can be done in terms of Lagrangian particle tracking, with particles traveling along different pathlines, which are the result of crossing different fractures and intersections until reaching the position $X$. The particle Lagrangian velocity is equal to the local Eulerian velocity along its travel. Each particle initially holds an amount of "charge" (mass or heat) that is equal to either the injected solute mass or the injected heat energy, divided by the number of particles $N$. This charge changes during the travel because of the diffusive exchange with the matrix. There is no mass or heat exchange between particle pathlines. This approach has been already adopted by a number of authors (Neretnieks, 1980; Yamashita & Kimura, 1990; Y. W. Tsang & Tsang, 2001; Painter & Cvetkovic, 2005). The change of charge is evaluated by solving the problem of advective transport with diffusion into matrix for the case of a single fracture (Tang et al., 1981), which, similar to Cvetkovic et al. (1999), we assimilate to a single pathline.

### 2.1. Transport in a Single Flow Path

Let $b(\ell)$ the fracture aperture along a single flow path, $\ell$ and $z$ the coordinates in the path longitudinal and transverse directions, respectively, while $t$ is time. Fluid flow is parallel to $\ell$ and defined by the flow velocity $v(\ell)$. According to this setting and to the hypotheses above, transport in the fracture is described by (Carrera et al., 1998)

$$b\frac{\partial F}{\partial t} + bv\frac{\partial F}{\partial \ell} = -2J, \tag{1}$$

where $F = F(\ell, t)$ represents the perturbation of either the fluid temperature $T$ or the fluid solute concentration $C$ in the fracture. In the first case the equation corresponds to the energy balance, in the second case to the mass balance. As specified above, we do not neglect solute diffusion for now. $J(\ell, t)$ is the diffusive flux that the fluid exchanges with the rock matrix per unit surface and per unitary fluid storage capacity, that is, porosity for solute and heat capacity for heat, which is defined as

$$J = -\xi D\frac{\partial F_m}{\partial z}\bigg|_{z=0}, \tag{2}$$

where $D$ is either the thermal or the molecular diffusion coefficient (or diffusivity) in the rock matrix, for the heat and solute transport, respectively. We assume $D$ as a constant for simplicity. The parameter $\xi$ expresses the ratio of matrix to fracture storage capacities, that is, the porosities for the solute transport problem and the heat capacities for the heat transport problem. The perturbation of temperature or solute concentration in the matrix, $F_m(\ell, z, t)$, is given by

$$\frac{\partial F_m}{\partial t} = D\frac{\partial^2 F_m}{\partial z^2} \tag{3}$$

Equations (1) and (3) are coupled by means of Equation (2), and they have to be solved together. Another coupling condition is defined by the continuity at the fracture wall, that is, $F_m(\ell, 0, t) = F(\ell, t)$, which defines a boundary condition (BC) for Equation (3). The other BC for the matrix equation is given by the hypothesis of infinite matrix. Without any loss of generality, we assume that the initial temperature and concentration are uniform in the system and equal to 0, both in the fractures and in the rock. We solve the problem of a pulse injection released at time $t = 0$ at one extreme of the fracture $\ell = 0$, which is also considered as infinite in the longitudinal direction. Therefore, the initial and BCs for the problem are

$$F_m(\ell, z, 0) = 0, \qquad F(\ell, 0) = 0 \tag{4}$$

$$F_m(\ell, 0, t) = F(\ell, t), \qquad F(0, t) = F_0\Delta t_0\delta(t) \tag{5}$$

$$F_m(\ell, \infty, t) = 0, \qquad F(\infty, t) = 0. \tag{6}$$

where $F_0$ denotes the temperature or the solute concentration released at the inlet, $\delta(t)$ is the Dirac function and $\Delta t_0$ represents the infinitesimal time of the pulse injection.

Solution of this problem at the outlet section $X$, corresponding to the pathline coordinate $L$, is (Cvetkovic et al., 1999)

$$\zeta(X,t) = \frac{F(L,t)}{(F_0 \Delta t_0)} = \frac{H(t-\tau)\lambda B}{\sqrt{\pi}(t-\tau)^{3/2}} \exp\left(-\frac{\lambda^2 B^2}{(t-\tau)}\right) \tag{7}$$

where $H(\cdot)$ is the Heaviside function, $\lambda = \xi\sqrt{D}$, while $\tau$ and $B$ represent the advective travel time and the flow wetted surface (Moreno & Neretnieks, 1993) from $\ell = 0$ to $\ell = L$, respectively

$$\tau = \int_0^L \frac{\mathrm{d}\ell}{v(\ell)} = \frac{L}{\langle v \rangle_s} \quad ; \quad B = \int_0^L \frac{\mathrm{d}\ell}{v(\ell) b(\ell)} = \int_0^\tau \frac{\mathrm{d}\tau'}{b(\tau')} = \frac{L}{\langle vb \rangle_s} = \frac{\tau}{\langle b \rangle_t}. \tag{8}$$

In Equation (8) we have introduced the space-weighted harmonic average and the time-weighted harmonic average, which are defined on each pathline, respectively, as

$$\langle y \rangle_s = \frac{\int_0^L \mathrm{d}\ell}{\int_0^L \frac{\mathrm{d}\ell}{y}} \quad ; \quad \langle y \rangle_t = \frac{\int_0^\tau \mathrm{d}\tau'}{\int_0^\tau \frac{\mathrm{d}\tau'}{y}}. \tag{9}$$

We name $\langle v \rangle_s$ and $\langle b \rangle_t$ as equivalent velocity and equivalent fracture aperture, respectively, because they will prove useful to fully characterize the observed transport response.

Note that the peak arrival time is $\sim\lambda^2 B^2 + \tau$, which means that the diffusion to the matrix causes a lag of $\lambda^2 B^2$ in the peak arrival time with respect to the pure advective transport (de La Bernardie et al., 2018). The peak value is instead equal to the inverse of the lag divided by $\sqrt{\pi}$. Thus, the peak value decreases with increasing diffusion coefficient, increasing travel time and decreasing fracture aperture. For very large time, the behavior is controlled by the first term of Equation (7), thus it exhibits a tail that scales with $t^{-3/2}$, which is the typical signature of advective transport into a single fracture adjacent to a semi-infinite diffusive matrix. When the matrix is instead of finite dimension, like in Sudicky and Frind (1982), the tail scales with a larger negative exponent that changes in time (Wang et al., 2020).

Solution of Equation (7) represents the probability for a particle to cross $x = X$ at the time $t$. In the absence of diffusion into the matrix, then $\zeta(X, t) = \delta(t - \tau)$, which means that the particle reaches $X$ at time equal to the advective time $\tau$ with probability 1. This condition also occurs for very small values of $\lambda^2 B^2$, that is, for small time or weak matrix diffusion (Hyman, Dentz, et al., 2019b). In the case of solute transport, the parameter $\lambda^2$ takes very small values for open fractures in rocks. In fact, assuming open fractures corresponds to fracture porosity equal to 1 and fracture thermal capacity equal to the water one (e.g., $\sim 4 \times 10^6$ J/m$^3$/K). With regard to the matrix, porosity can be very low in sedimentary or crystalline rocks (e.g., equal or smaller than 1%), while the rock thermal capacity is similar to the water one (e.g., $\sim 2 \times 10^6$ J/m$^3$/K). On the other hand, solute molecular diffusivity $D$ in rocks is of the order of $10^{-9}$ m$^2$/s, while thermal diffusivity is of the order or $10^{-6}$ m$^2$/s (De Marsily, 1986). We thus evaluate the parameter $\lambda^2$ as equal to $\sim 10^{-13}$ m$^2$/s for the solute transport, while it is $\sim 10^{-7}$ m$^2$/s for the heat. Based on these values, solute diffusion is disregarded here and the response to solute mass transport is assumed as equal to the advective response.

### 2.2. Transport in Multiple Flow Paths

The heterogeneity of a fracture system can be described similarly to the stochastic convective stream-tube approach, which has been widely adopted for the prediction of transport in highly heterogeneous fractured (Becker & Shapiro, 2003) and porous media (Cirpka & Kitanidis, 2000; Dagan & Bresler, 1979; Ginn et al., 1995; Simmons, 1982). There are $N$ pathlines in the system, each one characterized by single values of length $L$, travel time $\tau$ and flow wetted surface $B$, as defined in Equation (8). The observed response to transport at the control section is thus expressed as the average of the response over the pathline ensemble, such as

$$\overline{F}(X,t) = \frac{1}{N} \sum_{i=1}^{N} \zeta_i(X,t). \tag{10}$$

For the solute, we assume that the transport occurs mostly by advection, therefore the observation of the concentration $C$ will be solely the result of the variability of the advective travel time $\tau$. In other words, the observed BTC coincides with the probability density function (PDF, $\psi$) distribution of the advective travel time, as obtained by.

$$\overline{C}(X,t) = \int_0^\infty \zeta(X,t)\psi_\tau(\tau)\mathrm{d}\tau = \int_0^\infty \delta(t-\tau)\psi_\tau(\tau)\mathrm{d}\tau = \psi_\tau(t). \tag{11}$$

For the heat, the response to transport is affected by both the system heterogeneity and the diffusion to the rock matrix. Thus the solution to transport (Equation (10)) can be also expressed as

$$\overline{T} = \int_0^\infty \int_0^\infty \zeta(\tau, B)\psi_{\tau B}(\tau, B)\mathrm{d}\tau\mathrm{d}B, \tag{12}$$

where $\zeta(\tau, B)$ is the solution given in Equation (7) written in terms of Lagrangian quantities, while $\psi_{\tau B}(\tau, B)$ represents the joint probability of $B$ and $\tau$, which are strictly correlated. For sufficiently large times ($t \gg \tau$) we can disregard $\tau$ in $\zeta(\tau, B)$ such that Equation (12) is equivalent to

$$\overline{T} = \int_0^\infty \zeta(B)\psi_B(B)\mathrm{d}B. \tag{13}$$

Assuming that $B$ varies between a minimum and a maximum value, $B_m$ and $B_M$, respectively, and that its PDF distribution, $\psi_B(B)$, follows a power law (Painter et al., 2002) (see also Section 3.2.1), such as

$$\psi(B) = \frac{\gamma}{1-(B_M/B_m)^{-\gamma}}\frac{B^{-\gamma-1}}{B_m^{-\gamma}}, \tag{14}$$

the solution to Equation (13) is (Appendix A)

$$\overline{T} \approx \frac{\lambda}{\sqrt{\pi}}\begin{cases}\dfrac{\gamma}{\eta}\left[\dfrac{\lambda^{\gamma-1}}{2}\Gamma\left(\dfrac{1-\gamma}{2}\right)t^{-\gamma/2-1} - \dfrac{B_m^{1-\gamma}}{1-\gamma}t^{-3/2}\right] & , B_m^2 \ll \dfrac{t}{\lambda^2} \ll B_M^2 \\ \overline{B}t^{-3/2} & , \dfrac{t}{\lambda^2} \gg B_M^2\end{cases} \tag{15}$$

where $\eta = B_m^{-\gamma} - B_M^{-\gamma}$, and $\overline{B} = \gamma/(1-\gamma)\left(B_m^{1-\gamma} - B_M^{1-\gamma}\right)/\eta$ is the average value of $B$.

Equation (15) shows that the after-peak response follows two different regimes in time. For small times, that is, time between $\lambda^2 B_m^2$ and $\lambda^2 B_M^2$, the response is dominated by the aquifer heterogeneity and it scales with a power of time equal to $-\gamma/2 - 1$, if $\gamma$ is smaller than 1, otherwise it is dominated by diffusive behavior. At time equal to $\lambda^2 B_M^2$, the response starts to be completely diffusion dominated (it scales with $t^{-3/2}$), so we define this time as the onset of the asymptotic diffusive regime. Because of the combination of heterogeneity and diffusion effects, the tailing behavior does not correspond with the one defined by the pure advection, and it exhibits the characteristic diffusive scaling ($\propto t^{-3/2}$) only for late times.

In the following, we consider the heterogeneous setting described above ($N$ pathlines, each one characterized by single values of travel time $\tau$ and flow wetted surface $B$, and thus single values of equivalent fracture aperture $\langle b\rangle_t$) to analyze the response to pure advective transport and to advective transport with transverse diffusion for three extreme cases. The first one is the case of a system with homogeneous fracture aperture, the second is the case of parallel fractures in which travel time and equivalent fracture aperture of each pathline are perfectly correlated, the third is the case in which travel time and equivalent fracture aperture of each pathline are perfectly uncorrelated. The first two cases constitute end-members of a generic heterogeneous fractured system. The homogeneous case in fact corresponds to the case in which the flow converges into a few fractures because the network connectivity is low or it is dominated by large fractures. The parallel fracture case reflects instead a hyper-connected system or a system dominated by small fractures, in which the flow is capable to develop along the direction of the maximum potential. The third case represents an intermediate system in which connectivity dominates over the variability of the velocity field, such that travel time and aperture are perfectly uncorrelated.

### 2.2.1. Homogeneous Fracture Aperture

If the fracture aperture is homogeneous in the network, the response is completely determined by the velocity heterogeneity. In fact if $b$ is set as constant in Equation (8), then $B$ and the advective travel time $\tau$ are linearly

proportional, meaning that their variability is equal. We assume that this variability is described by an upper truncated power-law probability density function of the type

$$\psi(\tau) = \frac{\alpha}{1-(\tau_M/\tau_m)^{-\alpha}} \frac{\tau^{-\alpha-1}}{\tau_m^{-\alpha}} \tag{16}$$

where the subscript "$m$" and "$M$" refer to the minimum and maximum cutoff values, respectively, and where $\alpha > 0$ as conventionally observed in both porous and fractured media (e.g., Hyman, Dentz, et al., 2019a; Painter et al., 2002). In this case, and following Equation (15), the heat response exhibits the following decay rates

$$\overline{T} \propto \begin{cases} t < (\lambda B_M)^2 : & t^{-\alpha/2-1},\ \alpha < 1; \quad t^{-3/2},\ \alpha > 1 \\ t > (\lambda B_M)^2 : & t^{-3/2}. \end{cases} \tag{17}$$

where $(\lambda B_M)^2 = (\lambda \tau_M / b)^2$. This case has also been analyzed by Hyman, Dentz, et al. (2019b) for the case with no upper cutoff, that is, considering only the pre-asymptotic behavior. During this time, two different decay rates may be observed whether $\alpha$ is larger or smaller than 1.

#### 2.2.2. Parallel Fractures—Perfectly Correlated Travel Time and Equivalent Fracture Aperture

Let now consider a set of sub-parallel fractures extending from the inlet to the outlet with similar length $L$. This setting should not be confused with the well-known model analyzed by Sudicky and Frind (1982), in which transport occurs in a set of identical and equidistant parallel fractures. Here we assume that each fracture is characterized by an advective travel time $\tau$ and an equivalent aperture $\langle b \rangle_t$. For simplicity we assume that the aperture is roughly uniform along each fracture and equal to $\langle b \rangle_t$. Given the constant head BCs imposed at the fracture ends, and that the fractures do not intersect, then the cubic law implies that the equivalent flow velocity is exclusively depending on the square of the equivalent aperture, that is, $\langle v \rangle_s \propto \langle b \rangle_t^2$. Since we have assumed that the fracture aperture is uniform along each fracture, flow velocity is also uniform because they are perfectly correlated. Under this condition, for both aperture and velocity, the space-weighted harmonic average and the time-weighted harmonic average coincide, and they are equal to equivalent quantities and to the local ones, that is, $\langle y \rangle_s = \langle y \rangle_t = \langle y \rangle = y$. According with these relationships and Equation (8), the travel time is inversely proportional to the square of the equivalent aperture, while $B$ is inversely proportional to the cube of the equivalent aperture, such that

$$\tau \propto \langle b \rangle_t^{-2}; \quad B \propto \tau^{3/2}. \tag{18}$$

This means that if the advective travel time in the fracture system is distributed like in Equation (16), then $\psi(\langle b \rangle_t) \propto \langle b \rangle_t^{2\alpha-1}$ and $\psi(B) \propto B^{-2/3\alpha-1}$. Consequently, the observed heat response follows two different regimes in time

$$\overline{T} \propto \begin{cases} t < (\lambda B_M)^2 : & t^{-\alpha/3-1},\ \alpha < 3/2; \quad t^{-3/2},\ \alpha > 3/2 \\ t > (\lambda B_M)^2 : & t^{-3/2}. \end{cases} \tag{19}$$

where $B_M$ scales with $\tau_M^{3/2}$. Similar to the case of uniform aperture, the pre-asymptotic regime exhibits the diffusive signature ($t^{-3/2}$) only if $\alpha$ is smaller than a threshold value, in this case equal to 3/2.

It should be emphasized that in the case of parallel fractures with uniform aperture along each fracture, it is easy to relate the statistics of the equivalent quantities with the characteristics of the network. In fact, they are related through a flux weighted injection mode, that is, the number of pathlines on each fracture is proportional to the flux on the fracture itself. This allows to create a map between the statistics of the equivalent quantities and the statistics of the Eulerian fields (the field of aperture and velocity in the whole domain) such as (Dentz et al., 2016)

$$\psi(\langle y \rangle) = \frac{Q}{\overline{Q}} \psi(y_E) \tag{20}$$

where $Q$ is the injected flow rate in each fracture $Q = vb = \langle v \rangle \langle b \rangle \propto \langle v \rangle^{3/2}$ and $\overline{Q}$ is the average $Q$ over all the fractures. By applying this rule, and reminding that $\psi(\langle v \rangle) \propto \langle v \rangle^{\alpha-1}$, the Eulerian distribution of flow velocity and fracture aperture are expressed by $\psi(v_E) \propto v^{\alpha-5/2}$ and $\psi(b_E) \propto b^{2\alpha-4}$, respectively.

This case can be extended to any system with independent pathlines that do not cross each other. If the fracture aperture variation is little along each pathline, then the equivalent fracture aperture and the travel time are perfectly correlated. Therefore, the same considerations as above can be done.

#### 2.2.3. Perfectly Uncorrelated Travel Time and Equivalent Fracture Aperture

We consider here that the advective travel time $\tau$ and the equivalent fracture aperture $\langle b \rangle_t$ are independent and uncorrelated random variables, both distributed according with an upper truncated power-law probability density function. For the advective travel time, the distribution is as described by Equation (16) with positive values of $\alpha$, while for $\langle b \rangle_t$ we assume the following distribution

$$\psi(\langle b \rangle_t) = \frac{\beta}{(\langle b \rangle_{t,M} / \langle b \rangle_{t,m})^{\beta} - 1} \frac{\langle b \rangle_t^{\beta-1}}{\langle b \rangle_{t,m}^{\beta}}, \tag{21}$$

where the subscript "$m$" and "$M$" refer again to the minimum and maximum cutoff values, respectively. For the value of $\beta$ we keep the general assumption that it may be either larger or smaller than 1. Nevertheless, in Section 3 we will observe that $\beta > 1$ is largely observed in fractured media.

According with this framework, $B$ can be described as a random variable with double power-law distribution $\psi(B)$ (Appendix B), each branch defined by either the heterogeneity of $\tau$ or $\langle b \rangle_t$. Note that in the case of $\beta > \alpha$, $\psi(B)$ is defined by the $\tau$ heterogeneity for small $B$ values and by the $\langle b \rangle_t$ heterogeneity for large $B$ values. The opposite occurs if $\beta < \alpha$. We explore the different possibilities in the following.

Thus, the pre-asymptotic behavior (first line of Equation (15)) can be further expanded into two regimes in time, each one dominated by either the heterogeneity of $\tau$ or $\langle b \rangle_t$. For example, in the case of $\beta > \alpha$, the observed BTC is given by solving the integral of Equation (13) with $\psi(B)$ defined by Equation (B4), which gives

$$\overline{T} \approx \frac{\lambda}{\sqrt{\pi}} \begin{cases} \dfrac{\gamma'}{\eta_1}\left[\dfrac{\lambda^{\alpha-1}}{2}\Gamma\left(\dfrac{1-\alpha}{2}\right)t^{-\alpha/2-1} - \dfrac{B_m^{1-\alpha}}{1-\alpha}t^{-3/2}\right] & , B_m^2 \ll \dfrac{t}{\lambda^2} \ll B_0^2 \\ \overline{B_1}t^{-3/2} + \dfrac{\gamma'}{\eta_2}\left[\dfrac{\lambda^{\beta-1}}{2}\Gamma\left(\dfrac{1-\beta}{2}\right)t^{-\beta/2-1} - \dfrac{B_0^{1-\beta}}{1-\beta}t^{-3/2}\right] & , B_0^2 \ll \dfrac{t}{\lambda^2} \ll B_M^2 \\ \left(\overline{B_1} + \overline{B_2}\right)t^{-3/2} & , \dfrac{t}{\lambda^2} \gg B_M^2 \end{cases} \tag{22}$$

where $\gamma' = \alpha\beta/(\beta - \alpha)$, $\eta_1 = B_m^{-\alpha} - B_0^{-\alpha}$, $\eta_2 = B_0^{-\beta} - B_M^{-\beta}$, $\overline{B_1}$, and $\overline{B_2}$ are the average values of $B$ in the two branches of the PDF (see Appendix B), and

$$B_m = \frac{\tau_m}{\langle b \rangle_{t,M}}; \quad B_0 = \frac{\tau_M}{\langle b \rangle_{t,M}}; \quad B_M = \frac{\tau_M}{\langle b \rangle_{t,m}}. \tag{23}$$

Note that the smallest and the greatest time limits correspond to the extreme conditions of most and least advective-dominated transport, respectively. We can also reformulate the limits in terms of characteristic times. Let $t_{c,m} = \langle b \rangle_{t,m}^2 / \lambda^2$ and $t_{c,M} = \langle b \rangle_{t,M}^2 / \lambda^2$ as the minimum and the maximum diffusive characteristic times, while $\tau_m$ and $\tau_M$ are the minimum and maximum advective travel times, respectively. This allows to redefine the limits of Equation (22) such that time is compared to

$$\lambda^2 B_m^2 = \tau_m^2 / t_{c,M}; \quad \lambda^2 B_0^2 = \tau_M^2 / t_{c_M}; \quad \lambda^2 B_M^2 = \tau_M^2 / t_{c,m}. \tag{24}$$

When $\beta > \alpha$, the behavior is therefore summarized by

$$\overline{T} \propto \begin{cases} t < (\lambda B_0)^2 : & t^{-\alpha/2-1},\ \alpha < 1; \quad t^{-3/2},\ \alpha > 1 \\ (\lambda B_0)^2 < t < (\lambda B_M)^2 : & t^{-\beta/2-1},\ \beta < 1; \quad t^{-3/2},\ \beta > 1 \\ t > (\lambda B_M)^2 : & t^{-3/2} \end{cases} \tag{25}$$

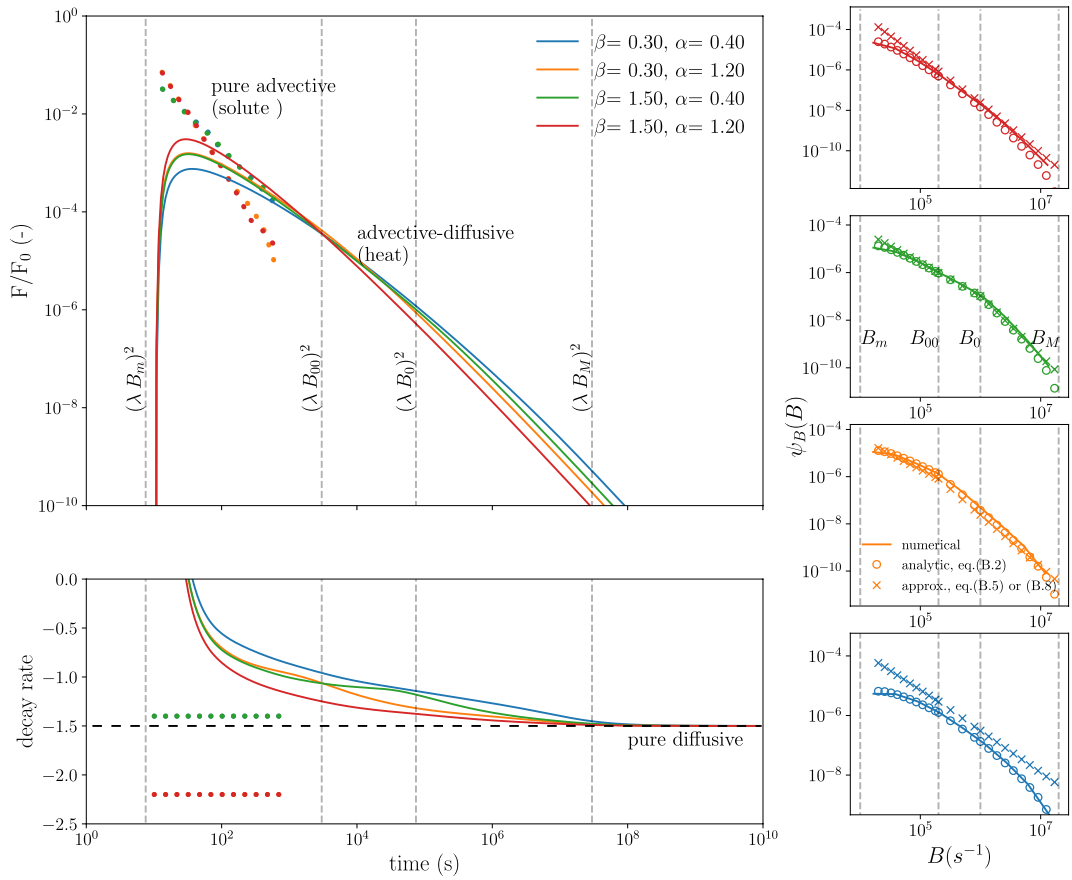


**Figure 1.** Results of numerical simulation of solute mass and heat transport, in the case of perfectly uncorrelated travel time and equivalent aperture, and under different scenarios of heterogeneity. Panels on the left-hand side show the observations in time at a control section for (upper panel) solute mass concentration (dotted lines) and temperature (solid lines), both normalized with respect to the value released at the inlet, and (lower panel) their decay rate with time, that is, the log-log derivative. Lines represent the average over the pathline solutions (Equation (10)). The vertical gray dashed lines represent the limits that define the three regimes. The intermediate limit is defined by either $B_0$ or $B_{00}$, whether $\beta$ is larger or smaller than $\alpha$, respectively. The horizontal black dashed line in the lower panel represents the typical diffusive behavior proportional to $t^{-3/2}$, which defines the asymptotic regime. The panels on the right-hand side show the PDF distribution of $B$ for the four scenarios of heterogeneity. Solid lines represent the values from the numerical simulation of the pathline ensemble, circle markers represent the analytic expression as derived in Equation (B2), while crosses represent the approximated expression as in Equation (B4) for $\beta > \alpha$, or Equation (B7) for $\beta < \alpha$.

while when $\beta < \alpha$, the behavior is summarized by

$$\overline{T} \propto \begin{cases} t < (\lambda B_{00})^2 : & t^{-\beta/2-1},\ \beta < 1; \quad t^{-3/2},\ \beta > 1 \\ (\lambda B_{00})^2 < t < (\lambda B_M)^2 : & t^{-\alpha/2-1},\ \alpha < 1; \quad t^{-3/2},\ \alpha > 1 \\ t > (\lambda B_M)^2 : & t^{-3/2}. \end{cases} \tag{26}$$

where $B_{00} = \tau_m / \langle b \rangle_{t,m}$.

Figure 1 shows an example of solute (pure advective) and heat (advective with transverse diffusion) transport under different scenarios of heterogeneity. We assume $\lambda^2 = 3 \times 10^{-7}$ m$^2$/s, $\tau_m = 10$ s, $\tau_M = 1{,}000$ s, $\langle b \rangle_{t,m} = 5 \times 10^{-5}$ m, $\langle b \rangle_{t,M} = 1 \times 10^{-3}$ m. Considering pathlines with a length of approximately 10 m, these values yield equivalent Peclet numbers ($Pe = \langle v \rangle_s \langle b \rangle_t / D$) ranging between 0.5 and 1,000. Two sets of values are assumed for both $\alpha$ and $\beta$. We consider an ensemble of $10^6$ pathlines and calculate the response according to Equation (10). The upper left panel shows the observations in time at a control section (BTC) while the lower left panel shows the temporal variation of the time decay rate of the response (the log-log derivative of the observations in time). For the solute

transport, the BTC curve is equivalent to the PDF distribution of the advective particle travel times $\psi_\tau(t)$ (Equation (16)). When diffusion into matrix is not disregarded, the response is delayed with respect to the advective response, and the peak occurs with a lag of approximately $\tau_m/\langle b\rangle_{t,M}$ with respect to the pure advective peak arrival time. Notice that we disregard $\tau$ in Equation (13). The peak value is greater for weak $\tau$ heterogeneity (larger $\alpha$) and $\beta > 1$, conditions that give raise to the highest probability density of the smallest $B$ (see also right panels).

After the peak, the heat response scales as a power of time according with different regimes (see bottom left panel), confirming the behavior predicted by the approximate solution of Equations (26) and (25). Before reaching the asymptotic diffusive regime, the tailing behavior is determined first by the heterogeneity of the travel time and then by the heterogeneity of the fracture aperture, if $\beta > \alpha$. The opposite occurs if $\beta < \alpha$. Observe that the approximation is more accurate when the difference between the values of $\beta$ and $\alpha$ is larger (orange and green lines), which is a consequence of the better approximation of $B$ with Equation (B4), or Equation (B7), for these cases (observe the right panels). The case with both $\alpha$ and $\beta$ larger than one quickly exhibits a decay rate equal to $-3/2$, because the diffusive response dominates in this case, whereas the case with both $\alpha$ and $\beta$ smaller than one exhibits diffusive behavior only for time larger than the diffusive behavior onset, that is, $(\lambda B_M)^2$, (compare the red and the blue lines).

#### 2.2.4. Comparison of Cases

We compare here the heat response for the three extreme cases illustrated above, to which we assign the short nomenclature of *homogeneous*, *parallel*, and *uncorrelated*. We assume that the three cases are characterized by the same distribution of $\tau$, that is, the solute BTC is the same. For the uncorrelated case the distribution of $\tau$ and $\langle b\rangle_t$ is like described in Section 2.2.3 with $\alpha = 0.4$ and $\beta = 1.5$. For the homogeneous and parallel cases the distribution of $\tau$ completely defines the distribution of $B$. The latter is generated assuming that the three cases have equal values of $B_m$, which is equivalent to analyze the three responses as non-dimensionalized with respect to the peak arrival time.

Figure 2 shows the BTC and decay rate evolution in time. The peak value and peak time are the same for the three cases, but the post-peak behavior differs. Initially, the tails for the uncorrelated and homogeneous cases have similar decay rate, while the parallel case one is slightly larger. They are all determined by the value of $\alpha$. This pre-asymptotic regime remains invariable for $t > (\lambda B_0)^2$ in the case of parallel fractures, while it changes in the other two cases. The homogeneous case shows diffusive behavior for shorter time than the other cases. The onset of the asymptotic regime is in fact corresponding with $B_0$. The uncorrelated case does not show a clearly defined decay rate, but rather a decreasing decay rate before reaching the characteristic diffusive scaling for $t > (\lambda B_M)^2$. This is due to the value of $\beta > 1$ (compare with Figure 1). The parallel case reaches the diffusive decay rate for $t > (\lambda B_0)^2 \tau_M/\tau_m$.

Taking into account the features described above, we can infer some important properties of the fractured medium, by the combined observation of solute and heat tracer tests. We will test these hypotheses against numerical simulations with DFN systems in the next section.

## 3. Numerical Analysis of Solute and Heat Transport in DFNs

We test our theoretical formulation against results of numerical experiments in DFNs. This allows for analyzing the link between the observations (BTC) and the network characteristics. We employ the simulator DFN.Lab (DFN. Lab, 2022; Goc et al., 2019; Pinier et al., 2022), a software platform that includes a set of modules for the generation of stochastic heterogeneous fracture networks, and for the modeling of flow and transport in the connected network.

### 3.1. Model Setup

#### 3.1.1. Network Generation and Characterization

The network is composed of randomly oriented disk-shaped fractures which are uniformly distributed over a cubic 3D domain with edge side equal to 10 m. The network is characterized by three major attributes. The first is the fracture size $d$, which is sampled from a truncated power law distribution with exponent $\omega$, such as

$$\psi_d(d) = \frac{\omega d_m^\omega}{1-(d_m/d_M)^\omega} d^{-\omega-1}, \tag{27}$$

where $\psi$ represents the probability density function (PDF), $d_m$ and $d_M$ represent the lower and upper cutoffs, respectively. We consider three different scenarios with values of $\omega$ equal to 1, 2, and 3. Extreme scenarios corresponds to networks where the fracture density is controlled by large ($\omega = 1$) or small fractures ($\omega = 3$) (Maillot

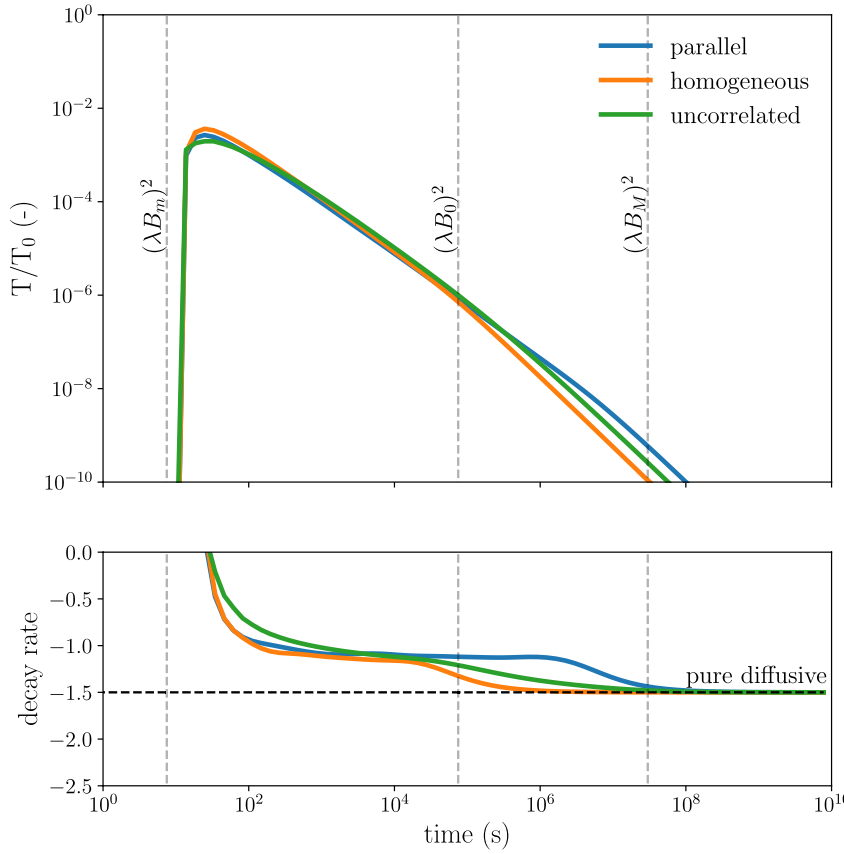


**Figure 2.** Temporal response to advective transport with transverse diffusion at a control section for the case of homogeneous fracture aperture, parallel fractures, and uncorrelated travel time and equivalent fracture aperture. Upper panel: temperature normalized with respect to the value released at the inlet; lower panel: decay rate of the response with time (log-log derivative). The vertical gray dashed lines represent the limits that define the three regimes for the uncorrelated case. The horizontal black dashed line in the lower panel represents the typical diffusive behavior with decay rate in time equal to −3/2, which defines the asymptotic regime.

et al., 2016). We set the values of the lower and upper cutoff equal to 0.1 m and 10, which correspond to ratios of 0.01 and 1, respectively, with respect to the domain size (Figure 3).

The second attribute is the fracture aperture $b$, which we consider as positively correlated with the fracture size, according to the power law relationship

$$b = b_0\left(\frac{d}{2}\right)^{\theta}. \tag{28}$$

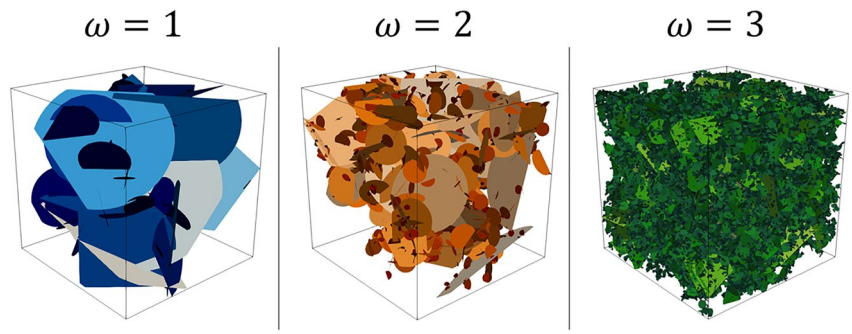


**Figure 3.** One example of DFN for each of the three different scenarios of fracture size distribution. The set of connected fracture is shown, with darker colors representing the smaller fractures.

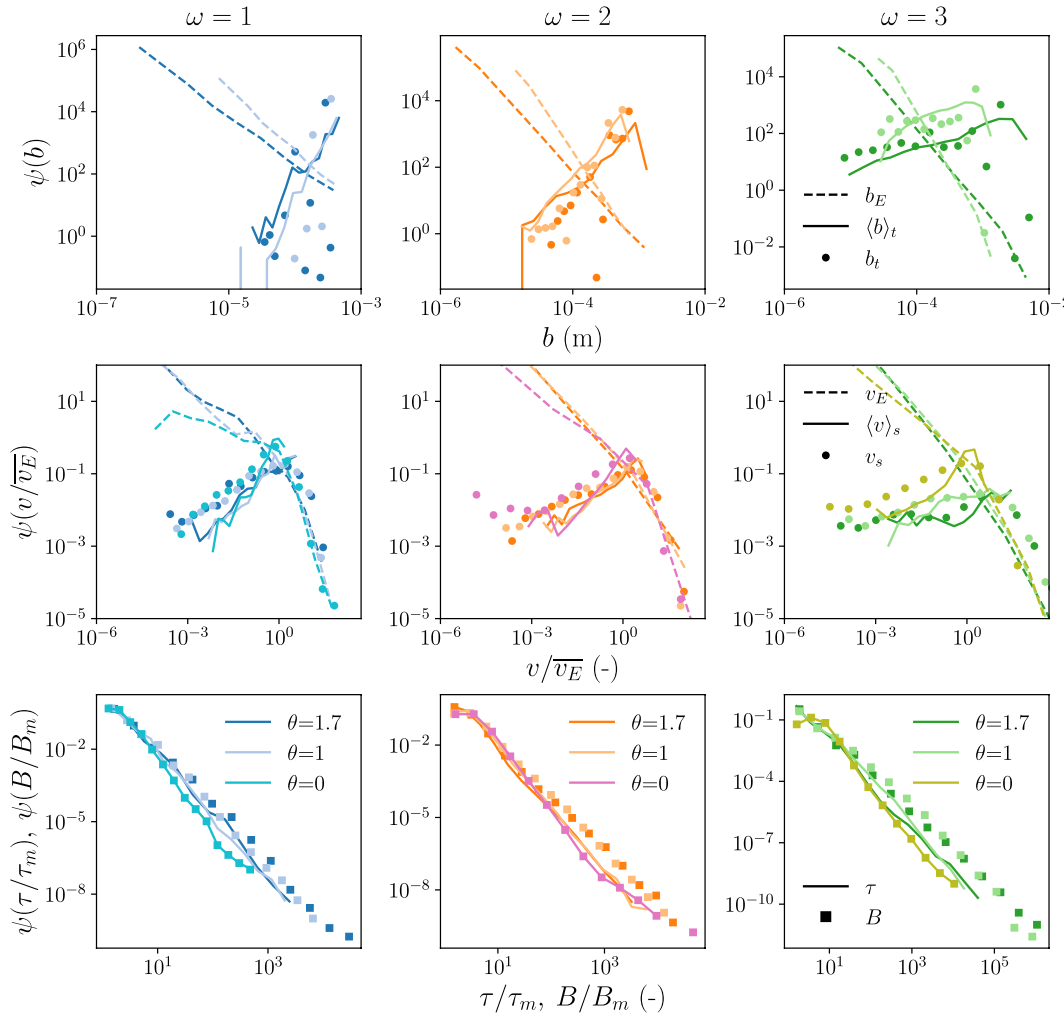


**Figure 4.** From top to bottom: comparison of PDF distributions of fracture aperture, velocity, advective travel time $\tau$ and flow wetted surface $B$ for all the scenarios, represented by different colors. In the top and middle rows, the dashed lines correspond to the Eulerian field, the solid lines to the equivalent parameters, that is, time-weighted harmonic average of aperture and space-weighted harmonic average of velocity, while the dot markers indicate the Lagrangian sampling, that is, isochronous for the fracture aperture and equidistant for the velocity. All velocities are normalized with respect to the average value in the Eulerian field for each scenario. In the bottom row, the advective travel time $\tau$ (solid lines) and the flow wetted surface $B$ (markers) are normalized with respect to their minimum value, for each scenario.

This is a common assumption in DFN models (de Dreuzy et al., 2002) and it reflects field observations of natural fractured aquifers (Renshaw & Park, 1997; Vermilye & Scholz, 1995). Scaling with exponent $\theta$ ranging from 0.5 (Walmann et al., 1996) to 2 (Hatton et al., 1994) have been reported (see also the discussion in Bonnet et al. (2001)). In this study, for each of the three scenarios of fracture length distribution, we consider values of $\theta$ equal to 0, 1 and 1.7, corresponding to networks with no, moderate or large variability of the fracture aperture, respectively. If $\theta = 0.5$ is instead adopted, like in Hyman, Dentz, et al. (2019b), the variability of the aperture is very little, and the results are similar to the ones obtained with $\theta = 0$. Equation (28) implies that the fracture aperture PDF is distributed according to a power law with exponent $-(\omega/\theta + 1)$. The slope of the PDF is thus different for each scenario, but the ranges of variability are the same, that is, approximately two and three orders of magnitude in the case with $\theta = 1$ and $\theta = 1.7$, respectively (Figure 4). Note that the assumption on the fracture aperture directly implies an assumption on the fracture transmissivity, as we consider the validity of the cubic law, that is, the fracture transmissivity is equal to $b^3/(12\mu)$, with $\mu$ representing the fluid viscosity (Witherspoon et al., 1980; Zimmerman & Bodvarsson, 1996). The parameter $b_0$ is set with a different value in each scenario, such that the average velocities are comparable (Table 1).

The third relevant attribute regards the fracture density and connection, which we define by means of the percolation parameter $p$, a measure of the volume of connected fractures over the total fracture volume (Bour &

**Table 1**
*Characteristics of the Fracture Network for Each of the Scenarios*

| $\omega$ (−) | $\theta$ (−) | $b_0 \times 10^{-4}$ m | Number of connected fractures |
|---|---|---|---|
| 1 | 1.7 | 0.4 | 46 |
| 1 | 1 | 1 | 46 |
| 1 | 0 | 5 | 46 |
| 2 | 1.7 | 2 | 1485 |
| 2 | 1 | 2 | 1485 |
| 2 | 0 | 5 | 1485 |
| 3 | 1.7 | 8 | 95,763 |
| 3 | 1 | 5 | 95,763 |
| 3 | 0 | 5 | 95,763 |

Davy, 1997). For a 3D domain of random disks, the value $p = 2.5$ constitutes a threshold for the generation of a connected system of fractures (de Dreuzy et al., 2000). We consider $p$ equal to 5 for all the modeled networks, corresponding to a moderately well connected aquifer.

The values of the setting and resulting parameters for all the considered scenarios are summarized in Table 1. For each scenario we generate and model 10 different realizations. For each fracture set, the network of connected fractures is determined, while isolated fractures are removed as they do not participate in the flow process (Figure 3).

#### 3.1.2. Flow and Transport

Fluid flow occurs exclusively in the fracture network and there is no interaction with the rock matrix, which is considered impervious. Under the assumptions of steady state, laminar flow with incompressible fluid, and assuming the validity of the cubic law, the flow is governed by

$$\nabla \cdot Q = \nabla \cdot \left( \frac{b^3}{12\mu} \nabla p \right) = 0, \tag{29}$$

where $Q$ represents the volumetric flow rate per unitary fracture lateral extension and $\nabla p$ represents the local pressure gradient. As described above, the transmissivity is constant within each fracture and proportional to its length. The forcing for flow is applied in the form of constant pressure BCs, and thus a pressure difference, between opposite faces in the $x$-direction, while no-flow conditions are applied on the other boundaries. The steady-state flow equation in the connected network is solved through a mixed hybrid finite element scheme (Goc et al., 2019; Pinier et al., 2022), which ensures fluid mass conservation, including for unstructured meshes with a high variability in element quality. The mesh is composed by triangles with an average size of 0.01 m and with smaller elements close to fracture intersections, where a minimum of two elements are generated at each intersection edge. Tests with a more refined mesh have proven that the chosen mesh size is sufficient to obtain accurate results. The linear system is solved by a LLT solver.

Transport is simulated via Lagrangian particle tracking, which solves the advective part of the problem, combined with Equation (7) to model the diffusive part along each pathline under the assumption of semi-infinite rock matrix. The diffusivity parameter is set as $\lambda^2 = 3 \times 10^{-7}$ m$^2$/s. We inject $5 \times 10^5$ particles which move by flow advection in the system of connected fractures. Results do not differ if a larger number of particles is introduced in the system. Particle injection follows a flux-weighted injection mode, which ensures a stationary distribution of Lagrangian velocities (Dentz et al., 2016). Full mixing is assumed at the fracture intersections.

### 3.2. Analysis of Results

#### 3.2.1. Flow and Transport Characteristics

In this section we analyze the impact of the network characteristics on the statistics of flow velocity, fracture aperture, travel time $\tau$ and flow wetted surface $B$ (Figure 4). We show here the detailed results of one realization for each scenario, while the results of the complete set of realizations is presented in Supporting Information S1. We differentiate between the Eulerian field, that is, the field of velocity and aperture in the whole domain, $v_E$ and $b_E$, and the Lagrangian field, that is, the velocity and aperture values visited by the particles. The latter can be sampled at fixed space jumps or at fixed travel time. For the velocity we show the Lagrangian equidistant sampling, for example, space-Lagrangian $v_s$, while for the aperture we show the Lagrangian isochronous sampling, for example, time-Lagrangian $b_t$. The steps for the sampling are set as 1 m and 1 s, respectively. Finally, we also analyze the PDF distribution of the equivalent parameters, that is, the space-weighted harmonic average of velocity $\langle v \rangle_s$, and the time-weighted harmonic average of fracture aperture $\langle b \rangle_t$ (Equation (9)). We analyze these quantities for the complete particle ensemble, which gives a more complete measure of the parameter statistics (Puyguiraud et al., 2019).

While for all scenarios the Eulerian PDF of fracture aperture is distributed as a power law with negative exponent (equal to $-(\omega/\theta + 1)$, as we discussed in Section 3.1.1), both the equivalent aperture and the time-Lagrangian sampling of the aperture exhibit power law PDFs with positive exponent, that is, the largest value is more

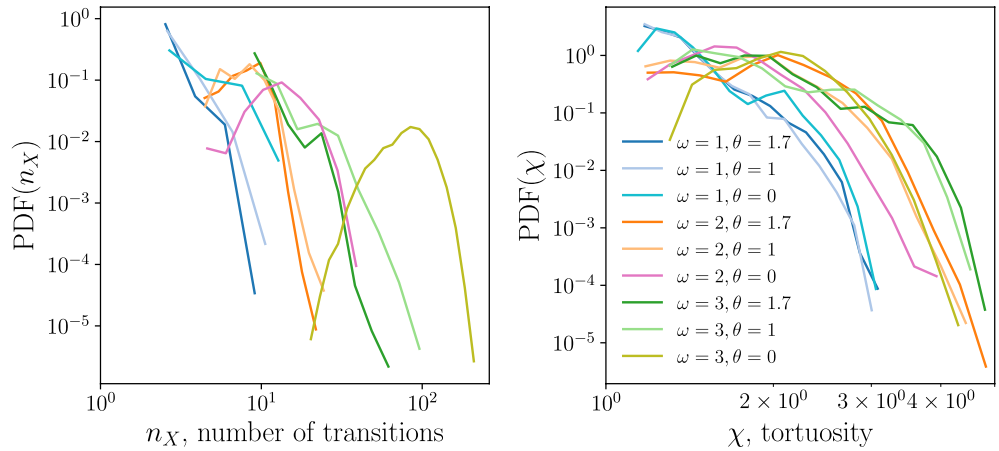


**Figure 5.** PDF distributions of (left) number of visited fractures, or transitions, and (right) tortuosity, for all particle pathlines from inlet to outlet. Colors correspond to different scenarios.

probable than the smallest one (top panels of Figure 4). That is a consequence of two factors. First, fracture size and aperture are positively correlated, which means that fractures with larger aperture are visited for longer time because of their larger size. They have, therefore, a larger weight in the definition of the equivalent aperture (Equation (9)). Second, fractures with larger aperture constitute preferential paths for flow, because they are characterized by higher flow rates. Note that the equivalent aperture and the time-Lagrangian aperture exhibit similar PDF distribution. Note also that the PDF distribution of $\langle b \rangle_t$ corresponds to values of $\beta$ larger than 1 if the expression of Equation (21) is assumed.

Although the Eulerian distributions of fracture aperture are not exactly the same for the three scenarios with different $\omega$ (recall also Section 3.1.1), the PDF of both the equivalent aperture and the time-Lagrangian aperture differ even more. The scenario with $\omega = 3$ exhibits the strongest variability, with smallest and largest values similar to the ones of the Eulerian field and with a more horizontal PDF distribution, revealing that many fractures are visited and the entire field is sampled as a consequence of the small size of fractures (see also Figure 5). When $\omega = 1$, the PDF distribution is very steep, and both the smallest visited (time-Lagrangian) aperture and the smallest equivalent aperture are much larger than the Eulerian smallest values, indicating that the flow concentrates along larger fractures with larger $b$, while smaller fractures are not visited. The scenario with $\omega = 2$ exhibits an intermediate behavior with a less pronounced under-sampling. With respect to $\theta$, we do not observe a clear impact on the distribution of the equivalent aperture.

The analysis of the flow velocity points out similar considerations (middle panels of Figure 4). The Eulerian velocity field shows a double-power distribution with larger negative decay rates for the large velocity than for the small ones, which is typically observed in fractured media (Hyman, Dentz, et al., 2019a). The space-Lagrangian velocity exhibit a similar distribution for the large values of velocity, while the small values, which determine the late-time passage times, exhibit a power law PDF with positive exponent. The relationship between these two statistics in porous or fractured media have been largely examined by Dentz et al. (2016); Comolli and Dentz (2017); Frampton and Cvetkovic (2007); Hyman, Rajaram et al. (2019); and Puyguiraud et al. (2019), as we further discuss in the Discussion section. However, the parameter that directly impacts the advective travel time is the equivalent velocity, that is, the space-weighted harmonic average $\langle v \rangle_s$. For all scenarios, its maximum value is much smaller than that of the Eulerian and space-Lagrangian distribution, and it coincides with the values with largest density of space-Lagrangian velocity. The distribution of $\langle v \rangle_s$ follows a power law with positive exponent, whose value decreases with increasing $\omega$. This behavior depends on the fact that the flow concentrates along preferential paths with higher velocity. This is particularly true when the network is composed by large fractures ($\omega = 1$), where indeed the number of transitions (visited fractures) and the tortuosity (total length of path divided by distance, $\chi = L/X$) are smaller (Figure 5). Comparing the three scenarios with different $\theta$, the cases with homogeneous fracture aperture ($\theta = 0$) exhibit steeper PDFs of $\langle v \rangle_s$ than the cases with variable fracture aperture. The latter ones do not show any clear difference between each other. According with the variability observed for the local (Lagrangian) and equivalent parameters, both the local ($Pe = vb/D$) and the equivalent Peclet numbers ($Pe = \langle v \rangle_s \langle b \rangle_t / D$) take values approximately between $10^{-3}$ and $10^4$.

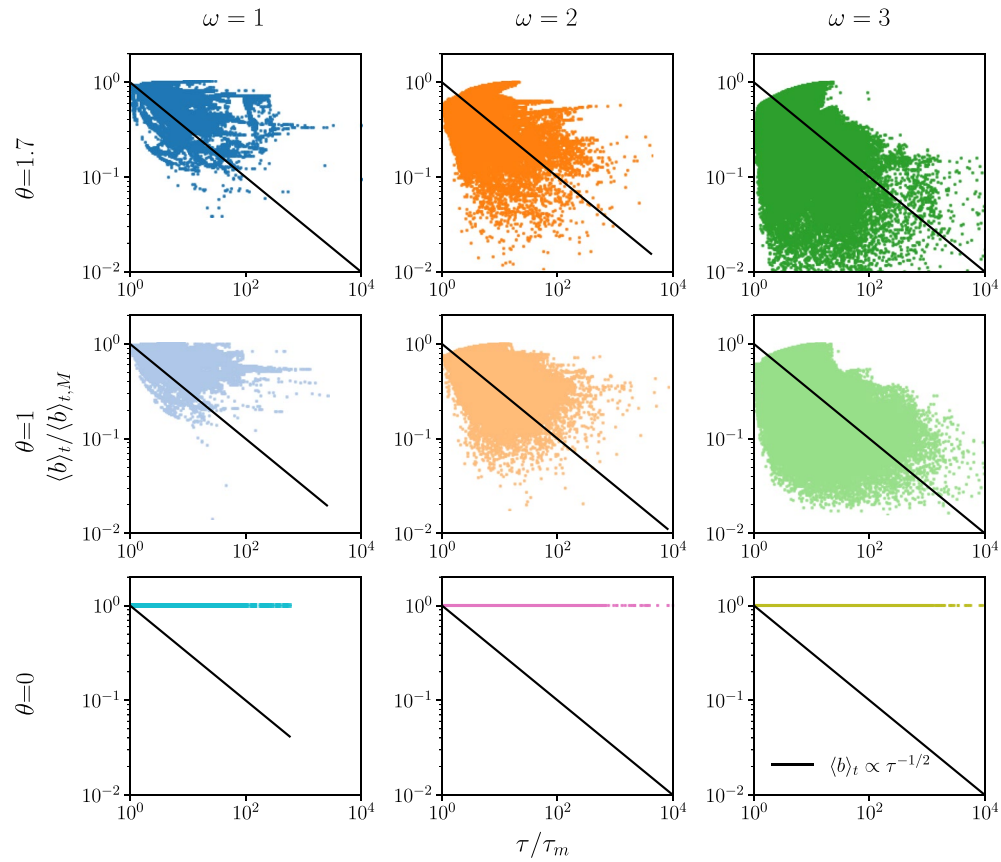


**Figure 6.** Correlation between travel time $\tau$, and equivalent fracture aperture $\langle b \rangle_t$, for each particle pathline from inlet to outlet, and for all scenarios. The black line indicates the correlation as per the cubic law, that is, corresponding to the parallel case hypothesis. Values are normalized with respect to the minimum travel time and maximum equivalent fracture aperture, respectively.

The distribution of equivalent velocity directly impacts the variability of the travel time $\tau$ and the flow wetted surface $B$ (bottom panels of Figure 4). The slope of the PDF of $\tau$ does not significantly change between the three scenarios, however the travel time varies over a larger range for high values of $\omega$ than for small values of $\omega$. Furthermore, when $\omega$ is small, $B$ is similar to $\tau$, indicating that the network behaves similar to the case with homogeneous fracture aperture, while when $\omega$ is larger, $B$ and $\tau$ differ more. This is a consequence of the larger variability of the equivalent aperture. We further analyze the variability of $B$ and $\tau$ in the following section.

### 3.2.2. Correspondence With Theoretical Considerations

According with the cubic law (Equation (29)), flow velocity is locally proportional to the square of the fracture aperture, $b^2$. This proportionality also applies to the equivalent quantities of velocity and fracture aperture when the pathlines are parallel (Section 2.2.2), that is, when the connectivity does not play any role. To verify if this condition occurs in a generic network, we analyze the correlation between $\tau$ and $\langle b \rangle_t$ in Figure 6, where each point represents the values of $\tau$ and $\langle b \rangle_t$ of one pathline. In fact, since tortuosity is small (Figure 5), we can neglect variations in the pathline lengths $L$, and assume that $\tau$ is equal to the inverse of the equivalent velocity $\langle v \rangle_s$. Although we can recognize a general correlation trend following the cubic law, that is, $\tau \propto \langle b \rangle_t^{-2}$, the data points largely spread around it, because the variability caused by connectivity effects is large and it dominates over the correlation, especially when $\omega$ is small (large fractures). When $\omega$ is large, the cubic relationship is more evident, suggesting that this case is closer to the parallel case.

The comparison between the numerical results from DFN simulations and the three theoretical cases proposed in Section 2.2 is performed in Figure 7, where the PDF distribution of $B$ is shown. For each scenario, the PDF of $B$ observed from numerical simulations are compared with the PDF of $B$ calculated from the observed $\tau$ and $\langle b \rangle_t$. In detail, $B$ is calculated as proportional to $\tau$ for the homogeneous case, to $\tau^{3/2}$ for the parallel case, and equal to

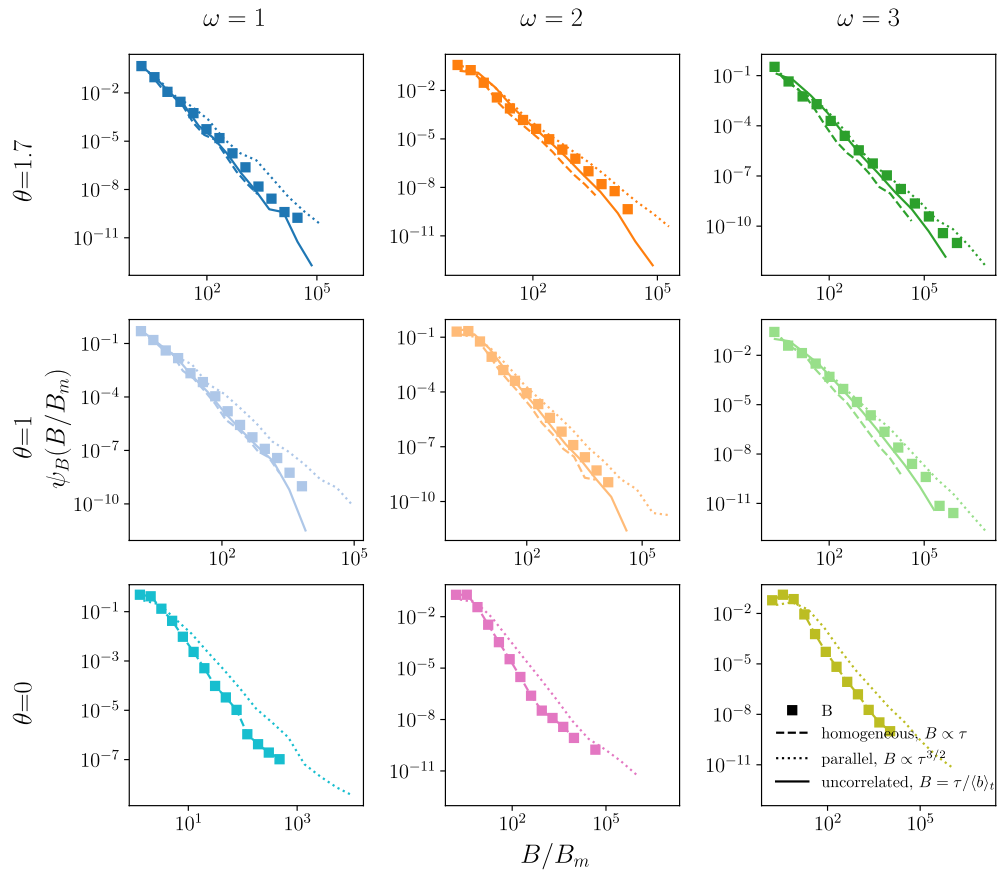


**Figure 7.** Probability density function of the flow wetted surface $B$ as observed from numerical simulations (markers) and estimated according with the theoretical assumption of homogeneous fracture aperture (dashed lines), parallel fractures (dotted lines) and perfectly uncorrelated $\tau$ and $\langle b \rangle_t$ (solid lines). Values of $B$ are normalized with respect to its minimum value for each scenario.

$\tau/\langle b \rangle_t$ for the uncorrelated case. Results show that the homogeneous and parallel cases constitute end members for the numerically estimated PDF of $B$. The PDF is underestimated if the homogeneous assumption is taken, while it is overestimated if the assumption of parallel fractures is considered. In general terms, the estimation of $B$ according with the assumption of uncorrelated $\tau$ and $\langle b \rangle_t$ provides better estimates of the variability of $B$, although it incurs an overestimation of the largest cutoff value, which can also be a consequence of an insufficient number of particles in the numerical simulations. Overall, the network composed by large fractures ($\omega = 1$) is closer to the homogeneous case, while the network composed by small fractures ($\omega = 3$) is closer to the parallel case assumption. In the next section we analyze the consequences of this features on the heat response.

### 3.2.3. BTC Observations and Interpretation

So far, we have mostly analyzed non-observable quantities that however directly impact the observable BTC. The heat response is indeed strictly related with the variability of $B$, while we assume that particle arrival time to the outlet, $\tau$, represents the solution for solute transport. Figure 8 shows the heat BTC for the different scenarios analyzed here, together with the solute response, which we already analyzed in Figure 4. The solute and heat BTC exhibit different peaks and tails. Since the pathline length $L$ is almost constant, $\tau$ depends exclusively on the harmonic average velocity $\langle v \rangle_s$, which is a function of connectivity and transmissivity variation. For the three scenarios of $\omega$, when the fracture aperture is homogeneous ($\theta = 0$), the temperature time decay rate rapidly evolves into the asymptotic diffusive behavior, that is, $-3/2$. This confirms the analysis of Sections 2.2.1 and 2.2.4, because the slope of the PDF of $\tau$ is larger than 2 (i.e., $\alpha > 1$). A similar behavior is observed when $\omega = 1$, for both the values of $\theta \neq 0$, reflecting that these cases are close to the homogeneous aperture case, as also expressed by the similarity between the PDF distributions of $B$ and $\tau$ that we observed in Figure 4. For larger $\omega$, the tail exhibits a decay rate smaller than $-3/2$, which is a consequence of the slope of PDF($B$) being smaller than 1.

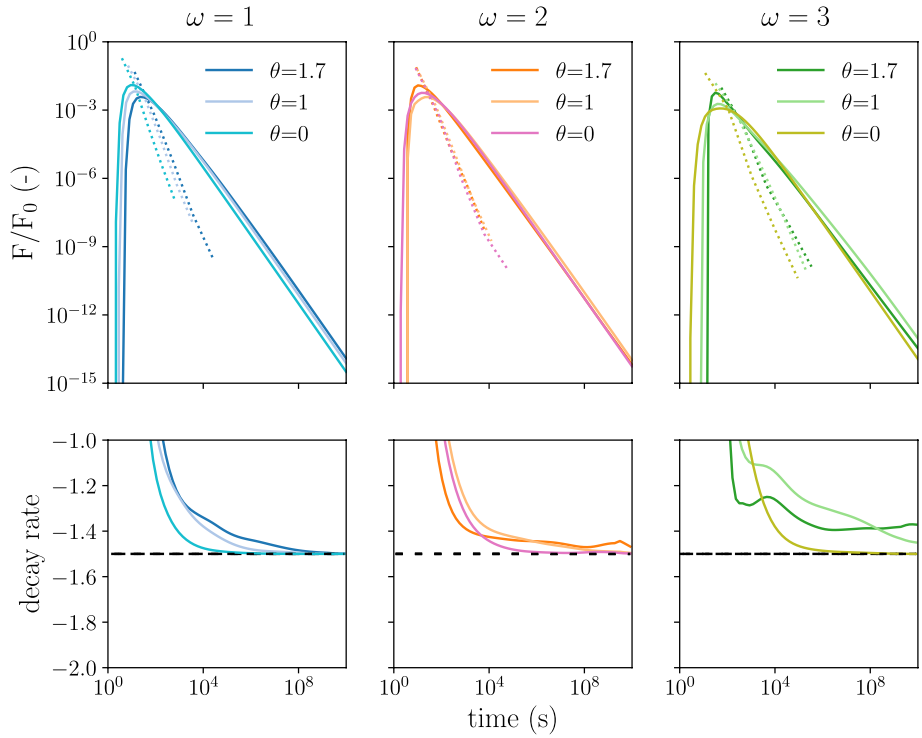


**Figure 8.** Temporal evolution of the heat (solid lines) and solute (dotted lines) breakthrough curve (BTC) observed at the outlet section (top), and of the slope of the heat BTC (bottom) for all the scenarios considered. The black dashed line in the bottom panels indicates the typical diffusive behavior with decay rate in time equal to −3/2.

From the combined observations of the solute and heat BTC, we attempt to back-calculate some of the upscaled network characteristics. For this analysis we refer to 10 realizations for each of the considered scenarios. First, the maximum equivalent aperture $\langle b \rangle_{t,M}$ is estimated from the observations of the peaks. The solute peak time corresponds to the fastest travel time $\tau_m$, while the thermal peak is delayed by $(\lambda B_m)^2 = (\lambda \tau_m / \langle b \rangle_{t,M})^2$ (see Section 2.2). From the lag of the thermal peak with respect to the solute peak, $t_p - \tau_m$, we can therefore derive $\langle b \rangle_{t,M} = \tau_m \lambda / \sqrt{t_p - \tau_m}$. Figure 9 (left panel) shows that in most cases the method provides quite good estimates if the true value of diffusivity $\lambda$ is adopted. Although the variability of this parameter is in general small in geological materials, we explore the uncertainty associated with the variability of $\lambda$ by considering values of thermal diffusion $D$ of one order of magnitude smaller and larger than the true one. This corresponds to estimation errors smaller than one order of magnitude because $\lambda \propto \sqrt{D}$ (observe the error bars).

Second, we infer the minimum equivalent aperture $\langle b \rangle_{t,m}$ under the three assumptions of homogeneous fracture aperture, parallel pathlines (perfectly correlated $\tau$ and $\langle b \rangle_t$), or perfectly uncorrelated $\tau$ and $\langle b \rangle_t$ (Figure 9, central panel). In the first case, $\langle b \rangle_{t,m}$ is just equal to $\langle b \rangle_{t,M}$. In the second case, it is derived from the arrival time observations and the previously estimated $\langle b \rangle_{t,M}$, such as $\langle b \rangle_{t,m} = \langle b \rangle_{t,M} \sqrt{\tau_m / \tau_M}$ (recall Section 2.2.2). In the third case, $\langle b \rangle_{t,m}$ is estimated from the observed time of transition to the diffusive behavior, that is, when the decay rate starts to be equal to −3/2, which is assumed as equal to $(\lambda B_M)^2 = (\lambda \tau_M / \langle b \rangle_{t,m})^2$ (recall Section 2.2.3). However, if the time of diffusive behavior onset is smaller than $(\lambda B_0)^2$, with $B_0 = \tau_M / \langle b \rangle_{t,M}$ calculated from the estimated $\langle b \rangle_{t,M}$, we consider that $\langle b \rangle_{t,m} = \langle b \rangle_{t,M}$. The parameter $\lambda$ is assumed like above and the same observations about the uncertainty are valid. Results (Figure 9, central panel) show that the assumption of parallel pathlines incurs an underestimation of the minimum equivalent aperture by several orders of magnitude, while the assumption of homogeneous aperture provides overestimated values. The assumption of uncorrelated $\tau$ and $\langle b \rangle_t$ gives the best estimates, although with a slight overestimation by approximately one order of magnitude, in agreement with the observations of Figure 7. Note that this analysis is performed assuming the ideal case of being able to observe a long tail in the solute BTC and the onset of the diffusive asymptotic decay rate in the heat BTC. However, we may not be able to observe the complete evolution of the tails in a field tracer test, because of the limits in the detection of small values.

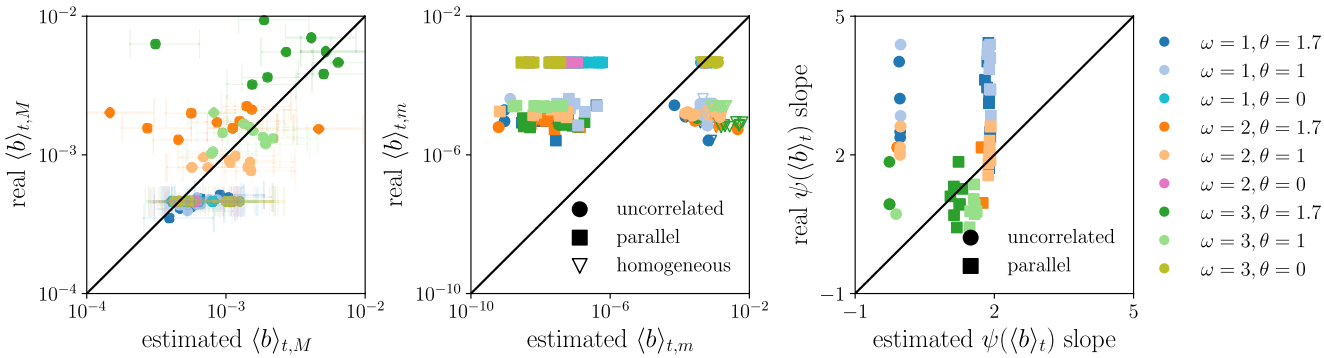


**Figure 9.** Estimated versus real values of (left) maximum, (center) minimum, and (right) slope of the PDF of $\langle b \rangle_t$ for several realizations of each scenario, represented by a different color. Estimated values are calculated from the observation of the solute and heat BTC as in Figure 8, while the real values are derived from the PDF as in Figure 4. The error bars in the left panel indicate the variability associated with assigning a value of the diffusion parameter $D$ spanning the range of one order of magnitude around the true value. The minimum $\langle b \rangle_t$ (center) is estimated under the hypothesis of homogeneous fracture aperture (triangles), parallel fractures (squares), or uncorrelated $\langle b \rangle_t$ and $\tau$ (circles). The slope of the PDF (right) is estimated considering parallel fractures, or uncorrelated $\langle b \rangle_t$ and $\tau$. Note that the estimation of $\langle b \rangle_{t,M}$ is independent of the hypothesis on the network structure.

Third, we estimate the slope of the equivalent aperture PDF, $\psi(\langle b \rangle_t)$, from the observed temperature decay rate $r$, under the two assumptions of parallel pathlines or uncorrelated $\tau$ and $\langle b \rangle_t$ (Figure 9, right panel). For the parallel case, we take the average decay rate for times larger than the peak time and smaller than the onset of diffusive behavior, and we apply the scaling of Equation (19) together with the one of Equation (18). For the uncorrelated case, we take the average decay rate for times larger than $B_0$ and smaller than the onset of diffusive behavior, and we apply the scaling of Equation (26). These estimations are compared against the real slope, which is derived directly from the PDF (as in Figure 4) by performing a weighted average to smooth out the oscillations. Results show that the parallel assumption provides good estimates of the slope of $\psi(\langle b \rangle_t)$ for the scenarios with large $\omega$, which is in agreement with observations of Section 3.2.2. For small $\omega$ the slope is instead underestimated. The uncorrelated assumption underestimates the slope of $\psi(\langle b \rangle_t)$ for any value of $\omega$, although we have observed that it gives good estimates of $B$ under different network scenarios (Figure 7). This discrepancy is caused by the fact that diffusion dominates for positive slopes ($\beta > 1$, recall Equation (26)) thus it is not possible to distinguish a clear decay rate smaller than $-3/2$ (see Figure 8).

Based on these observations, we claim that in the case of observing the characteristic diffusive tail for times just after $(\lambda B_0)^2$, we can argue that the variance of $\langle b \rangle_t$ is very small, which may coincides with the presence of a preferential flow path in a system constituted by large fractures. On the other hand, comparing solute and heat decay rates it is possible to determine how much the system is close to the parallel fracture case, which corresponds to a network composed by small fractures. These considerations bring us to define two indicators describing how much the system is close to the homogeneous case or the parallel fractures cases. The indicator of homogeneous behavior (or flow channeling), $I_h$, is estimated as the ratio of the observed post-peak heat decay rate to the diffusive decay rate $-3/2$

$$I_h = \frac{r(t > t_p)}{-3/2}. \tag{30}$$

The indicator of parallel pathlines, $I_p$, is estimated as the ratio of the observed post-peak heat decay rate to $-\alpha/3 - 1$, where $-\alpha - 1$ is the decay rate of the solute BTC (recall Equation (19))

$$I_p = \frac{r(t > t_p)}{-\alpha/3 - 1}. \tag{31}$$

Values of either $I_h$ or $I_p$ close to 1 are expressions of systems constituted by large or small fractures, respectively. Figure 10 shows the values of the two indicators as a function of the slope of $\psi(\langle b \rangle_t)$, which is inversely proportional to the power of the fracture size distribution $\omega$ (Figure 4), and thus to fracture size heterogeneity. The cases with imposed homogeneous fracture aperture ($\theta = 0$) are indicated for infinite values of slope of $\psi(\langle b \rangle_t)$ in the right-end side of the plots. $I_h$ is far from 1 for large $\omega$ and small slopes, while it approaches 1 for increasing slopes. For most realizations of the scenarios with $\omega = 1$ and $\theta = 1$, and for all the cases with $\theta = 0$, $I_h$ is precisely equal

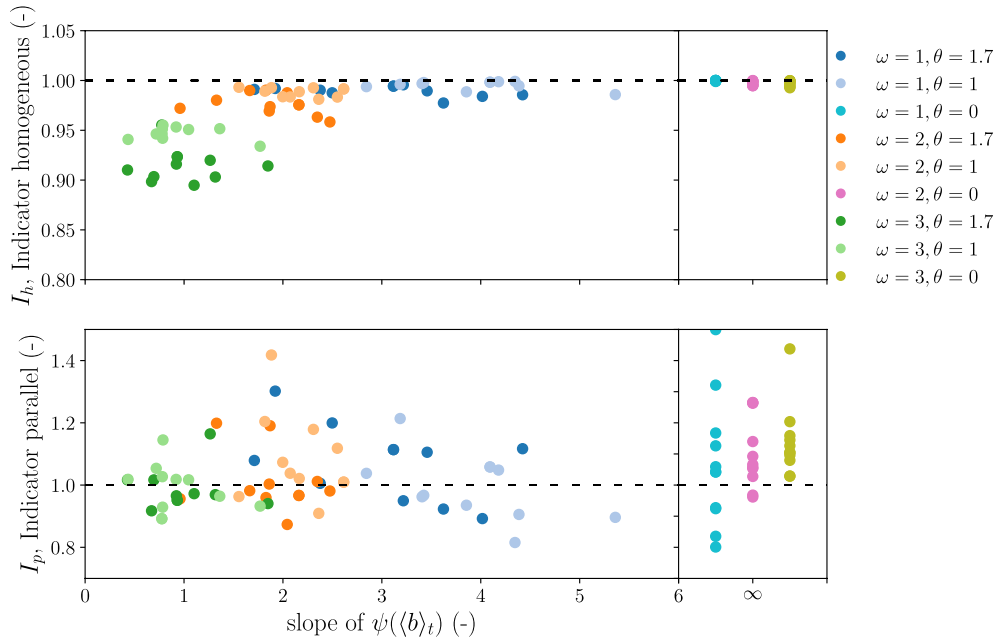


**Figure 10.** Indicators of the network structure as a function of the slope of $\psi(\langle b \rangle_t)$, which is inversely proportional to the heterogeneity of the fracture size. (top) $I_h$, indicator of networks composed by large fractures that concentrate flow, constituting systems with almost homogeneous fracture aperture. (bottom) $I_p$, indicator of networks composed by small connected fractures, constituting systems with almost parallel pathlines. The cases with imposed homogeneous fracture aperture ($\theta = 0$) are represented in the right end side of the plots. Dots represent different realizations with the color indicating the different network scenarios, as indicated in the legend that refers to both subplots.

to 1. $I_p$ is close or equal to 1 for small slopes, while it diverges from 1 for most cases with large slopes (note that the average deviation from 1 increases when moving from scenarios with $\omega = 3$ to the ones with $\omega = 1$). For the cases with $\theta = 0$, $I_p$ is far from 1 in most cases.

## 4. Discussion and Conclusions

We have investigated how the fluid-rock diffusive exchange impacts heat transport in heterogeneous fractured networks. We focused on the post-peak tail of the observed BTC, which can be described by means of a transition of power law distributions. We show that there is a time regime in which the decay rate may differ from the classical signature of matrix diffusion, that is, −3/2, before reaching the diffusive regime. This pre-asymptotic deviation from −3/2 expresses the heterogeneity of both flow velocity and fracture aperture in the network. In systems with homogeneous fracture aperture, the deviation occurs only when the advective transport is such that the distribution of the travel time decays slowly ($\alpha < 1$), as also shown by Hyman, Rajaram et al. (2019). When the fracture aperture is heterogeneous, the heterogeneity of the fracture aperture combines with the one of the advective travel time. Similar to Hyman et al. (2016) and Hyman and Dentz (2021), we illustrate that a unique value of equivalent aperture can be assigned to each of the trajectories. By using theoretical considerations, we estimate the post-peak decay rate for the case in which this equivalent aperture is perfectly correlated with the trajectory travel time, like in the ideal case of sub-parallel pathlines, and for the case in which the equivalent aperture is instead completely uncorrelated from the trajectory travel time, which we associate with a system where the connectivity effect dominates.

We have compared these theoretical results with results from numerical experiments on stochastically generated DFNs. These numerical simulations provide an in-depth view of the processes, as they allow analyzing the variability of the involved parameters, and compare them with the transport observables. For both velocity and fracture aperture, there is a significant difference between the Eulerian and Lagrangian statistics, because the particle trajectories are biased toward fractures with high flow rates (Frampton & Cvetkovic, 2007). This results in difficult-to-predict statistics of the equivalent Lagrangian quantities. Several approaches have been proposed to create a mapping that relates the Eulerian and Lagrangian fields, for example, velocity weighted mapping

algorithm (Comolli & Dentz, 2017; Dentz et al., 2016; Puyguiraud et al., 2019). They require the calibration of a few constraining parameters and in general apply to ergodic systems, that is, the whole variability is sampled. Invoking ergodicity, Hyman, Dentz et al. (2019b) attempt to reproduce the advective travel time PDF by adopting a stochastic convective stream-tube approach and assigning to each particle trajectory the velocity value assumed at the inlet section, which implies the underlying assumptions that the space averaged velocity $\langle v \rangle_s$ has the same PDF distributions of the velocity sampled at the same location over the particle ensemble.

However, ergodicity is not always fulfilled and the variability of the system is under-sampled because flow channelizes (Figure 4). Therefore, we do not attempt to describe the Eulerian fields of velocity and fracture aperture, but we analyze the BTC observations to characterize the network in terms of upscaled equivalent parameters, that is, advective travel time $\tau$, equivalent aperture $\langle b \rangle_t$, and flow wetted surface $B = \tau / \langle b \rangle_t$. Several authors investigated the correlation between $\tau$ and $B$, showing that the correlation is close to linear if the fracture size and aperture are correlated (Cvetkovic et al., 1999; Painter & Cvetkovic, 2005). Here, we confirm these results and we further investigate it, by analyzing also the correlation between $\tau$ and $\langle b \rangle_t$. In this context, the cubic relationship between flow velocity and fracture aperture is often invoked and extended to the equivalent velocity characterizing each of the multiple pathlines/channels (Becker & Shapiro, 2003) of the network. After doing so, a relationship of the kind $\tau \propto \langle b \rangle_t^{-2}$, and thus $B \propto \tau^{-3}$, is observed. However, in networks with complex topology, this proportionality is weak and the velocity mostly depends on the connectivity (Bour & Davy, 1998), as confirmed by the results from our numerical simulations (Figure 6). Similar to Cheng et al. (2003), we observe that the heterogeneity of a generic fractured system is bounded by two end-member situations. In one case, the equivalent velocity is exclusively a function of the fracture aperture, corresponding to the assumption of perfectly correlated travel time and equivalent aperture through the cubic relationship (Section 2.2.2). In the other case, the equivalent velocity is exclusively a function of the network connectivity. In this case, either the travel time and equivalent aperture are uncorrelated (Equation (22) applies), either the equivalent aperture is almost homogeneous (Section 2.2.1). The two cases constitute bounds for the numerical results. We observe that networks with larger fractures ($\omega = 1$) behave similar to the case with homogeneous fracture aperture, because the aperture variability is undersampled due to the fact that the flow channelizes along a small number of fractures. On the opposite side, when the network is composed by small fractures ($\omega = 3$), the behavior is closer to the hypothesis of parallel pathlines. Overall, we observe that the assumption of uncorrelated $\tau$ and $\langle b \rangle_t$ better captures the variability of $B$.

Based on these understandings, we have shown that it is possible to derive information on the fracture system from the combined observation of the solute and heat BTC. In particular, we are able to estimate the values of the maximum and minimum equivalent aperture, and in certain conditions the variability of the equivalent aperture, in systems where the variability of fracture aperture is large (Figure 9). Moreover, these observations allow us to characterize the connectivity structure. We have defined two indicators to distinguish whether the system is composed by small or large fractures, and to determine if the flow is concentrated along preferential paths (Figure 10).

It is worth emphasizing that we have analyzed the response to pulse injections of solute mass and heat, while in practice a continuous injection is performed for a short time. This implies a larger peak, which improves the detection, but it does not affect the decay rate which remains the same as for the pulse injection. Yet, late time pre-asymptotic and asymptotic tails may fall below the detection limit, which hinders the adoption of the proposed interpretation method.

This study allows us to illustrate the key features of diffusive transport in fractured heterogeneous systems, and their correspondence with characteristics of the fracture networks. Although we are not always able to interpret the observed results, this study constitutes a significant step in quantifying the upscaled characteristics of the fractured reservoirs that govern heat transport from the observation of BTCs. This is key during both design and management of subsurface applications, such as geothermal systems. Future works will investigate the impact of diffusion in systems with different levels of connectivity, as well as in different configurations of tracer tests.

## Appendix A1: Approximate Solution for Heterogeneous Diffusive Transport

The integral of Equation (13), with $\zeta$ defined in Equation (7) assuming $t \gg \tau$ and $\psi_B(B)$ expressed by Equation (B4), writes

$$\overline{T}(t) = \int_{B_m}^{B_M} \frac{\gamma}{\eta} \frac{\lambda}{\sqrt{\pi}} \frac{B^{-\gamma}}{t^{3/2}} \exp\left(-\frac{\lambda^2 B^2}{t}\right) dB, \tag{A1}$$

where $\eta = B_m^{-\gamma} - B_M^{-\gamma}$. Its solution is given by

$$\overline{T}(t) = -\frac{\gamma}{\eta}\frac{\lambda^{\gamma}}{2\sqrt{\pi}}t^{-\gamma/2-1}\left[\Gamma\left(\frac{1-\gamma}{2}, \frac{\lambda^2 B^2}{t}\right)\right]_{B_m}^{B_M}, \tag{A2}$$

where $\Gamma$ represents the incomplete gamma function.

We consider the two limits of the incomplete gamma function argument going respectively to $\infty$ and to 0, and we take the first order approximation, which returns

$$\lim_{x\to\infty}\Gamma(a,x) = 0 \tag{A3}$$

$$\lim_{x\to 0}\Gamma(a,x) = -\frac{x^a}{a} + \Gamma(a). \tag{A4}$$

Two regimes in time can be identified. For $\lambda^2 B_m^2 \ll t \ll \lambda^2 B_M^2$, we take the limit at $\infty$ for $B = B_M$, while the limit at 0 for $B = B_m$; for $t \gg \lambda^2 B_M^2$, we take the limits at 0 for both $B = B_M$ and $B = B_m$. Thus, we derive the approximate solution given in Equation (15).

## Appendix B1: Probability Density Functions for $B = \tau/\langle b\rangle_t$ with Perfectly Uncorrelated $\tau$ and $\langle b\rangle_t$

Reminding that, if $X$ and $Y$ are two independent continuous random variables with PDF functions $\psi_X(x)$ and $\psi_Y(y)$, the probability density function (PDF) of $Z = X/Y$ is

$$\psi_Z(z) = \int_{-\infty}^{\infty}\psi_X(zy)\psi_Y(y)\,|y|\,dy, \tag{B1}$$

and considering the PDF distributions of $\tau$ and $\langle b\rangle_t$ (Equations (16) and (21), respectively), we can derive the PDF for $B = \tau/\langle b\rangle_t$ as

$$\psi(B) = \frac{\alpha\beta\Lambda^{-1}}{(\beta-\alpha)}\begin{cases} B_0^{\alpha}\left(B^{-\alpha-1} - B_m^{\beta-\alpha}B^{-\beta-1}\right) & \text{if } B_m < B \le \min(B_0, B_{00}) \\ B_0^{\alpha}\left(B_0^{\beta-\alpha} - B_m^{\beta-\alpha}\right)B^{-\beta-1} & \text{if } B_0 \le B \le B_{00} \\ B_0^{\beta}\left(B_0^{-(\beta-\alpha)} - B_M^{-(\beta-\alpha)}\right)B^{-\alpha-1} & \text{if } B_{00} \le B \le B_0 \\ B_0^{\beta}\left(B^{-\beta-1} - B_M^{-(\beta-\alpha)}B^{-\alpha-1}\right) & \text{if } \max(B_0, B_{00}) \le B < B_{\max} \end{cases}, \tag{B2}$$

where $\Lambda = \left((B_0/B_m)^{\alpha} - 1\right)\left(1 - (B_0/B_M)^{\beta}\right)$ and

$$B_m = \frac{\tau_m}{\langle b\rangle_{t,M}}; \quad B_0 = \frac{\tau_M}{\langle b\rangle_{t,M}}; \quad B_{00} = \frac{\tau_m}{\langle b\rangle_{t,m}}; \quad B_M = \frac{\tau_M}{\langle b\rangle_{t,m}}. \tag{B3}$$

We immediately recognize that the first and last expressions of Equation (B2) define the probability for small and large values of $B$, respectively, while for intermediate values the second either the third expression holds, that is, whether $B_0 < B_{00}$ or $B_0 > B_{00}$.

Equation (B2) can be simplified acknowledging that $B_m \ll B$ and $B_M \gg B$ for $B < B_0$ and $B > B_0$, respectively. In the case of $\beta > \alpha$, the simplified solution is

$$\psi(B) \approx \frac{\alpha\beta}{(\beta-\alpha)}\begin{cases} \dfrac{B^{-\alpha-1}}{B_m^{-\alpha} - B_0^{-\alpha}} & \text{if } B_m \ll B \le B_0 \\ \dfrac{B_0^{\beta-\alpha}B^{-\beta-1}}{B_m^{-\alpha} - B_0^{-\alpha}} & \text{if } B_0 \le B \ll B_M \end{cases}. \tag{B4}$$

Notice that $\Lambda$ has been simplified assuming that the second term is equal to 1 as $B_M \gg B_0$.

The PDF of $B$ is thus distributed as a double power law. For values of $B$ smaller than $B_0$, the PDF is defined by the PDF of the travel time, while for values of $B$ larger than $B_0$, it is affected by the probability distribution of the

fracture aperture. $B_m$ and $B_M$ constitutes the lower and upper cutoffs, while the average values in the two branches of the PDF are, respectively

$$\overline{B_1} = \frac{\alpha}{\alpha - 1} \frac{B_m^{-\alpha+1} - B_0^{-\alpha+1}}{B_m^{-\alpha} - B_0^{-\alpha}} \tag{B5}$$

$$\overline{B_2} = \frac{\beta}{\beta - 1} \frac{B_0^{-\beta+1} - B_M^{-\beta+1}}{B_0^{-\beta} - B_M^{-\beta}}. \tag{B6}$$

In the case that $\beta < \alpha$, the simplified solution is instead

$$\psi(B) \approx -\frac{\alpha\beta}{(\beta - \alpha)} \begin{cases} \dfrac{B_m^{\beta-\alpha} B^{-\beta-1}}{B_m^{-\alpha} - B_0^{-\alpha}} & \text{if } B_m \ll B \leq B_{00} \\ \dfrac{(B_0/B_M)^{\beta-\alpha} B^{-\alpha-1}}{B_m^{-\alpha} - B_0^{-\alpha}} & \text{if } B_{00} \leq B \ll B_M \end{cases}. \tag{B7}$$

## Data Availability Statement

All materials, including scripts, input and output files, are available at the repository https://doi.org/10.5281/zenodo.6841355 (DeSimone, 2022). DFN.Lab is developed at the Fractory group (https://fractorylab.org/), a joint laboratory between the CNRS, the university of Rennes 1 and Itasca Consultants s.a.s. Details on the use and availability of the software are available at https://gitlab.com/fractorylab/dfnlab (DFN.Lab, 2022).

**Acknowledgments**
The authors acknowledge financial support from the SAD-GEOTHERM project (SAD18007) funded by the Brittany Region (France) under the SAD2018 framework.

## References

Becker, M. W., & Shapiro, A. M. (2000). Tracer transport in fractured crystalline rock: Evidence of nondiffusive breakthrough tailing. *Water Resources Research*, *36*(7), 1677–1686. https://doi.org/10.1029/2000wr900080

Becker, M. W., & Shapiro, A. M. (2003). Interpreting tracer breakthrough tailing from different forced-gradient tracer experiment configurations in fractured bedrock. *Water Resources Research*, *39*(1). https://doi.org/10.1029/2001wr001190

Berkowitz, B., & Scher, H. (1995). On characterization of anomalous dispersion in porous and fractured media. *Water Resources Research*, *31*(6), 1461–1466. https://doi.org/10.1029/95wr00483

Bonnet, E., Bour, O., Odling, N. E., Davy, P., Main, I., Cowie, P., & Berkowitz, B. (2001). Scaling of fracture systems in geological media. *Reviews of Geophysics*, *39*(3), 347–383. https://doi.org/10.1029/1999rg000074

Bour, O., & Davy, P. (1997). Connectivity of random fault networks following a power law fault length distribution. *Water Resources Research*, *33*(7), 1567–1583. https://doi.org/10.1029/96wr00433

Bour, O., & Davy, P. (1998). On the connectivity of three-dimensional fault networks. *Water Resources Research*, *34*(10), 2611–2622. https://doi.org/10.1029/98wr01861

Carrera, J., Sánchez-Vila, X., Benet, I., Medina, A., Galarza, G., & Guimerà, J. (1998). On matrix diffusion: Formulations, solution methods and qualitative effects. *Hydrogeology Journal*, *6*(1), 178–190. https://doi.org/10.1007/s100400050143

Cheng, H., Cvetkovic, V., & Selroos, J. O. (2003). Hydrodynamic control of tracer retention in heterogeneous rock fractures. *Water Resources Research*, *39*(5). https://doi.org/10.1029/2002wr001354

Cirpka, O. A., & Kitanidis, P. K. (2000). Characterization of mixing and dilution in heterogeneous aquifers by means of local temporal moments. *Water Resources Research*, *36*(5), 1221–1236. https://doi.org/10.1029/1999wr900354

Comolli, A., & Dentz, M. (2017). Anomalous dispersion in correlated porous media: A coupled continuous time random walk approach. *The European Physical Journal B*, *90*(9), 166. https://doi.org/10.1140/epjb/e2017-80370-6

Comolli, A., Hidalgo, J. J., Moussey, C., & Dentz, M. (2016). Non-fickian transport under heterogeneous advection and mobile-immobile mass transfer. *Transport in Porous Media*, *115*(2), 265–289. https://doi.org/10.1007/s11242-016-0727-6

Cvetkovic, V., Selroos, J. O., & Cheng, H. (1999). Transport of reactive tracers in rock fractures. *Journal of Fluid Mechanics*, *378*, 335–356. https://doi.org/10.1017/s0022112098003450

Dagan, G., & Bresler, E. (1979). Solute dispersion in unsaturated heterogeneous soil at field scale: I. Theory. *Soil Science Society of America Journal*, *43*(3), 461–467. https://doi.org/10.2136/sssaj1979.03615995004300030008x

De Dreuzy, J.-R., Davy, P., & Bour, O. (2000). Percolation parameter and percolation-threshold estimates for three-dimensional random ellipses with widely scattered distributions of eccentricity and size. *Physical Review E*, *62*(5), 5948–5952. https://doi.org/10.1103/physreve.62.5948

De Dreuzy, J.-R., Davy, P., & Bour, O. (2002). Hydraulic properties of two-dimensional random fracture networks following power law distributions of length and aperture. *Water Resources Research*, *38*(12), 121–1. https://doi.org/10.1029/2001wr001009

Dejam, M., Hassanzadeh, H., & Chen, Z. (2014). Shear dispersion in a fracture with porous walls. *Advances in Water Resources*, *74*, 14–25. https://doi.org/10.1016/j.advwatres.2014.08.005

De La Bernardie, J., Bour, O., Borgne, T. L., Guihéneuf, N., Chatton, E., Labasque, T., & Gerard, M.-F. (2018). Thermal attenuation and lag time in fractured rock: Theory and field measurements from joint heat and solute tracer tests. *Water Resources Research*, *54*(12). https://doi.org/10.1029/2018wr023199

De Marsily, G. (1986). *Quantitative hydrogeology: Groundwater hydrology for engineers*. Academic Press.

Dentz, M., Gouze, P., Russian, A., Dweik, J., & Delay, F. (2012). Diffusion and trapping in heterogeneous media: An inhomogeneous continuous time random walk approach. *Advances in Water Resources*, *49*, 13–22. https://doi.org/10.1016/j.advwatres.2012.07.015

Dentz, M., Kang, P. K., Comolli, A., Borgne, T. L., & Lester, D. R. (2016). Continuous time random walks for the evolution of Lagrangian velocities. *Physical Review Fluids*, *1*(7), 074004. https://doi.org/10.1103/physrevfluids.1.074004

De Simone, S. (2022). Materials for advective-diffusive transport in fractured media. *Computational Notebook, Datase*t. https://doi.org/10.5281/zenodo.6841355

DFN.Lab. (2022). Software. Retrieved from https://gitlab.com/fractorylab/dfnlab

Frampton, A., & Cvetkovic, V. (2007). Upscaling particle transport in discrete fracture networks: 1. Nonreactive tracers. *Water Resources Research*, *43*(10). https://doi.org/10.1029/2006wr005334

Frampton, A., Hyman, J. D., & Zou, L. (2019). Advective transport in discrete fracture networks with connected and disconnected textures representing internal aperture variability. *Water Resources Research*, *55*(7), 5487–5501. https://doi.org/10.1029/2018wr024322

Ginn, T. R., Simmons, C. S., & Wood, B. D. (1995). Stochastic-convective transport with nonlinear reaction: Biodegradation with microbial growth. *Water Resources Research*, *31*(11), 2689–2700. https://doi.org/10.1029/95wr02179

Goc, R. L., De Dreuzy, J.-R., & Davy, P. (2010). Statistical characteristics of flow as indicators of channeling in heterogeneous porous and fractured media. *Advances in Water Resources*, *33*(3), 257–269. https://doi.org/10.1016/j.advwatres.2009.12.002

Goc, R. L., Pinier, B., Darcel, C., Lavoine, E., Doolaeghe, D., Simone, S. D., & Davy, P. (2019). Dfn.lab: Software platform for discrete fracture network models. *AGU Fall Meeting*.

Haggerty, R., & Gorelick, S. M. (1995). Multiple-rate mass transfer for modeling diffusion and surface reactions in media with pore-scale heterogeneity. *Water Resources Research*, *31*(10), 2383–2400. https://doi.org/10.1029/95wr10583

Haggerty, R., McKenna, S. A., & Meigs, L. C. (2000). On the late-time behavior of tracer test breakthrough curves. *Water Resources Research*, *36*(12), 3467–3479. https://doi.org/10.1029/2000wr900214

Hatton, C. G., Main, I. G., & Meredith, P. G. (1994). Non-universal scaling of fracture length and opening displacement. *Nature*, *367*(6459), 160–162. https://doi.org/10.1038/367160a0

Hyman, J. D., Aldrich, G., Viswanathan, H., Makedonska, N., & Karra, S. (2016). Fracture size and transmissivity correlations: Implications for transport simulations in sparse three-dimensional discrete fracture networks following a truncated power law distribution of fracture size. *Water Resources Research*, *52*(8), 6472–6489. https://doi.org/10.1002/2016wr018806

Hyman, J. D., & Dentz, M. (2021). Transport upscaling under flow heterogeneity and matrix-diffusion in three-dimensional discrete fracture networks. *Advances in Water Resources*, *155*, 103994. https://doi.org/10.1016/j.advwatres.2021.103994

Hyman, J. D., Dentz, M., Hagberg, A., & Kang, P. K. (2019a). Emergence of stable laws for first passage times in three-dimensional random fracture networks. *Physical Review Letters*, *123*(24), 248501. https://doi.org/10.1103/physrevlett.123.248501

Hyman, J. D., Dentz, M., Hagberg, A., & Kang, P. K. (2019b). Linking structural and transport properties in three-dimensional fracture networks. *Journal of Geophysical Research: Solid Earth*, *124*(2), 1185–1204. https://doi.org/10.1029/2018jb016553

Hyman, J. D., Rajaram, H., Srinivasan, S., Makedonska, N., Karra, S., Viswanathan, H., & Srinivasan, G. (2019c). Matrix diffusion in fractured media: New insights into power law scaling of breakthrough curves. *Geophysical Research Letters*, *46*(23), 13785–13795. https://doi.org/10.1029/2019gl085454

Kang, P. K., Hyman, J. D., Han, W. S., & Dentz, M. (2020). Anomalous transport in three-dimensional discrete fracture networks: Interplay between aperture heterogeneity and injection modes. *Water Resources Research*, *56*(11). https://doi.org/10.1029/2020wr027378

Klepikova, M. V., Borgne, T. L., Bour, O., Dentz, M., Hochreutener, R., & Lavenant, N. (2016). Heat as a tracer for understanding transport processes in fractured media: Theory and field assessment from multiscale thermal push-pull tracer tests. *Water Resources Research*, *52*(7), 5442–5457. https://doi.org/10.1002/2016wr018789

Maillot, J., Davy, P., Goc, R. L., Darcel, C., & De Dreuzy, J. (2016). Connectivity, permeability, and channeling in randomly distributed and kinematically defined discrete fracture network models. *Water Resources Research*, *52*(11), 8526–8545. https://doi.org/10.1002/2016wr018973

Makedonska, N., Hyman, J. D., Karra, S., Painter, S. L., Gable, C. W., & Viswanathan, H. S. (2016). Evaluating the effect of internal aperture variability on transport in kilometer scale discrete fracture networks. *Advances in Water Resources*, *94*, 486–497. https://doi.org/10.1016/j.advwatres.2016.06.010

Méheust, Y., & Schmittbuhl, J. (2001). Geometrical heterogeneities and permeability anisotropy of rough fractures. *Journal of Geophysical Research*, *106*(B2), 2089–2102. https://doi.org/10.1029/2000JB900306

Moreno, L., & Neretnieks, I. (1993). Flow and nuclide transport in fractured media: The importance of the flow-wetted surface for radionuclide migration. *Journal of Contaminant Hydrology*, *13*(1–4), 49–71. https://doi.org/10.1016/0169-7722(93)90050-3

Neretnieks, I. (1980). Diffusion in the rock matrix: An important factor in radionuclide retardation? *Journal of Geophysical Research*, *85*(B8), 4379–4397. https://doi.org/10.1029/jb085ib08p04379

Painter, S., & Cvetkovic, V. (2005). Upscaling discrete fracture network simulations: An alternative to continuum transport models. *Water Resources Research*, *41*(2). https://doi.org/10.1029/2004wr003682

Painter, S., Cvetkovic, V., & Selroos, J. O. (2002). Power-law velocity distributions in fracture networks: Numerical evidence and implications for tracer transport. *Geophysical Research Letters*, *29*(14), 201–1. https://doi.org/10.1029/2002gl014960

Pinier, B., Goc, R. L., & Davy, P. (2022). Computation of flow and transport properties on large 3d heterogeneous stochastic and semi-deterministic fractured media with the platform dfn.lab. *In prep*.

Puyguiraud, A., Gouze, P., & Dentz, M. (2019). Stochastic dynamics of Lagrangian pore-scale velocities in three-dimensional porous media. *Water Resources Research*, *55*(2), 1196–1217. https://doi.org/10.1029/2018wr023702

Renshaw, C. E. (1995). On the relationship between mechanical and hydraulic apertures in rough-walled fractures. *Journal of Geophysical Research*, *100*(B12), 24629–24636. https://doi.org/10.1029/95JB02159

Renshaw, C. E., & Park, J. C. (1997). Effect of mechanical interactions on the scaling of fracture length and aperture. *Nature*, *386*(6624), 482–484. https://doi.org/10.1038/386482a0

Roubinet, D., De Dreuzy, J.-R., & Tartakovsky, D. M. (2012). Semi-analytical solutions for solute transport and exchange in fractured porous media. *Water Resources Research*, *48*(1). https://doi.org/10.1029/2011wr011168

Simmons, C. S. (1982). A stochastic-convective transport representation of dispersion in one-dimensional porous media systems. *Water Resources Research*, *18*(4), 1193–1214. https://doi.org/10.1029/wr018i004p01193

Sudicky, E. A., & Frind, E. O. (1982). Contaminant transport in fractured porous media: Analytical solutions for a system of parallel fractures. *Water Resources Research*, *18*(6), 1634–1642. https://doi.org/10.1029/wr018i006p01634

Tang, D. H., Frind, E. O., & Sudicky, E. A. (1981). Contaminant transport in fractured porous media: Analytical solution for a single fracture. *Water Resources Research*, *17*(3), 555–564. https://doi.org/10.1029/wr017i003p00555

Tsang, C. F., & Neretnieks, I. (1998). Flow channeling in heterogeneous fractured rocks. *Reviews of Geophysics*, *36*(2), 275–298. https://doi.org/10.1029/97rg03319

Tsang, Y. W., & Tsang, C. F. (2001). A particle-tracking method for advective transport in fractures with diffusion into finite matrix blocks. *Water Resources Research*, *37*(3), 831–835. https://doi.org/10.1029/2000wr900367

Vermilye, J. M., & Scholz, C. H. (1995). Relation between vein length and aperture. *Journal of Structural Geology*, *17*(3), 423–434. https://doi.org/10.1016/0191-8141(94)00058-8

Walmann, T., Malthe-Sørenssen, A., Feder, J., Jøssang, T., Meakin, P., & Hardy, H. H. (1996). Scaling relations for the lengths and widths of fractures. *Physical Review Letters*, *77*(27), 5393–5396. https://doi.org/10.1103/physrevlett.77.5393

Wang, L., Cardenas, M. B., Zhou, J.-Q., & Ketcham, R. A. (2020). The complexity of nonlinear flow and non-Fickian transport in fractures driven by three-dimensional recirculation zones. *Journal of Geophysical Research: Solid Earth*, *125*(9). https://doi.org/10.1029/2020jb020028

Witherspoon, P. A., Wang, J. S. Y., Iwai, K., & Gale, J. E. (1980). Validity of cubic law for fluid flow in a deformable rock fracture. *Water Resources Research*, *16*(6), 1016–1024. https://doi.org/10.1029/wr016i006p01016

Yamashita, R., & Kimura, H. (1990). Particle-tracking technique for nuclide decay chain transport in fractured porous media. *Journal of Nuclear Science and Technology*, *27*(11), 1041–1049. https://doi.org/10.1080/18811248.1990.9731289

Zimmerman, R. W., & Bodvarsson, G. S. (1996). Hydraulic conductivity of rock fractures. *Transport in Porous Media*, *23*(1). https://doi.org/10.1007/bf00145263